

Chapter 6

International Treaty Agreement to Build D–T Fusion Power Reactor Producing a Tokamak with Output Power 10X the injected heating power

6.1 The Technical Design Effort and Cost to Build a Power-producing Plasma — Like a star — in the Laboratory Led to the ITER Treaty

6.1.1 Steady-state lower-hybrid RF current drive produces steady-state plasmas eliminating runaway electrons

To maintain steady-state or hour-long pulse-fusion plasmas, one must use high-power RF driven waves launched from antennas along the vessel walls. The first successful steady-state toroidal plasmas were demonstrated in Tore Supra using Lower Hybrid Current Drive (LHCD). The steady-state experiments are described and reviewed in Chapter 13 of *Turbulent Transport in Magnetized Plasmas*, 2nd Ed., Horton (2018) ISBN:978-981-3225-86-6.

Long-pulse tokamak operation requires the change from the inductive transformer-driven toroidal electric field to steady-state plasmas with radio frequency RF antennas for driving the plasma current. The most effective RF current driver for the development of a fusion power reactor is the Lower Hybrid Current Drive (LHCD).

The first phase of plasma formation with inductive start-up electric fields from the tokamak transformer shows the development of electron distribution functions with parallel momentum electron groups that are continuously accelerated by the inductive electric fields. The energy gain of these runaway electrons must be terminated or controlled by RF waves tuned to push the relativistic electrons to the radial edge of the trapped plasma through the magnetic separa-

trix [Fontanilla and Breizman (2017), Breizman and Aleynikov (2017)]. Without control of the runaway electrons, severe damage to the metal vessel wall occurs.

The RF current drive works from wall-mounted antennas with large phased arrays of $TE_{1,0}$ wave guides that launch focused quasi-electrostatic 3-5 GHz lower hybrid plasma waves at about one-half the speed of light in the direction opposite to the toroidal plasma current. Modeling of the LHCD with the Tore Supra group [Horton, et al. (2013)] and continuing this work for the Tungsten Environment in Steady-State Tokamak (WEST) and Experimental Advanced Superconducting Tokamak (EAST) tokamaks [Horton, et al. (2017) *Santa Monica RF Conference*] explains the measured toroidal plasma currents.

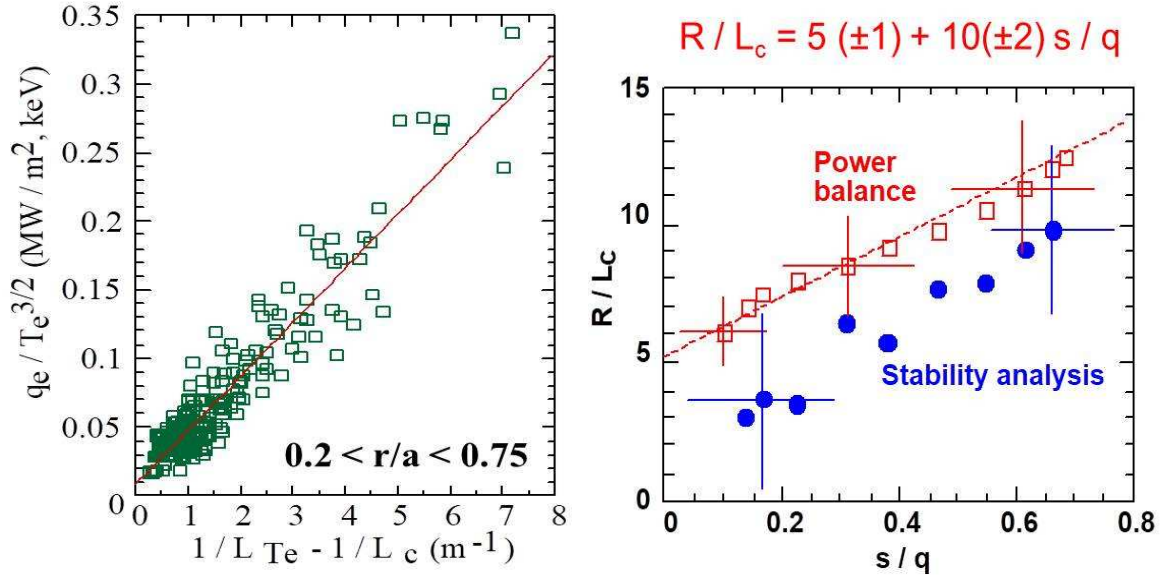


Figure 6.1: Simulation of Fast-Wave Heating with ETG Transport in Tore Supra.

Work continues on understanding the (LHCH) experiments with a magnetic separatrix that isolates the wall plasma from the hot core plasma. The WEST machine is a modification of Tore Supra with tungsten chamber walls inserted to model the walls needed for a reactor at a small scale. New issues arose in attempting to reproduce the earlier results from Tore Supra with circular flux surfaces. WEST has a lower single-null tungsten divertor which makes the modeling and dynamics more complex. Simulation codes take into account the wall shape and the X-point on the separatrix [Horton, et al., *Santa Monica Proceedings of RF Conference* (2017), Aix-en-Provence, June (2017) to model WEST and EAST [Goniche, et al. (2019), Decker, et al. (2011), Peysson, et al. (2011, 2016), Goniche, et al. (2019), Hoang, et al. (2003), Horton, et al. (2013a,b, 2017)].

For steady-state or long-pulse tokamak operation Lower-Hybrid Current Drive (LHCD) is required and the extended, asymmetric electron distribution $f_e(p_{\parallel}, p_{\perp}, r, t)$ changes the stability of the Electron Temperature Gradient (ETG) turbulence driven by fast electrons. This interaction modifies both electron current-carrying distribution function and the state of the ETG plasma

turbulence. The ETG turbulence also scatters the RF waves used in the diagnostics systems essential to measuring and controlling the tokamak plasma.

Wall erosion from the multi-KeV electron plasmas driven for minutes by the Klystrons is observed and requires further investigation. Full wave codes and RF ray simulation codes are used to test the theoretical formulas derived for steady-state RF operation. Modeling includes the angle scattering of the RF rays off the low-frequency drift wave turbulence that is modified by the anisotropic electron momentum distributions that extend from $3-4v_e$ up to the antenna-launched RF phase velocity at approximately one-half the speed of light. Examples of the plasma turbulence producing the RF wave scattering are shown in Fig. 6.2.

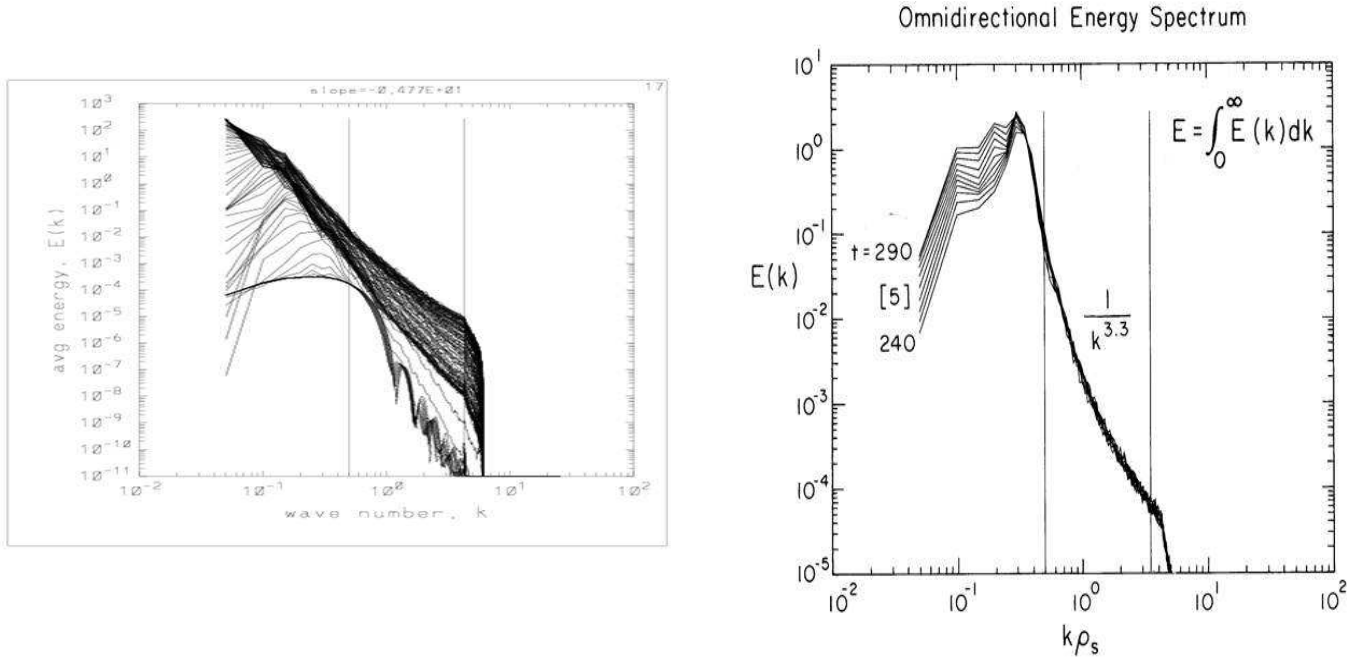


Figure 6.2: Inverse cascade from ρ_e to ρ_s and c/ω_{pe} of the plasma turbulence.

Density fluctuations from the ETG-driven drift waves scatter the gigaHertz RF waves from the slow wave polarization (quasi-electrostatic lower hybrid wave) into the fast wave — or whistler — RF wave polarization. The density fluctuation scattering and the coupling of the slow to the fast RF waves is computed and gives RF spectra closer to those measured in WEST and EAST than calculations without the RF scattering.

Secondly, the importance of including the scattering of the launched RF waves into the longer wavelength fast waves is that the scattering increases the RF current drive in the core plasma. The core current drive is missed by models that only follow the launched slow RF waves. Both simulations and data for the WEST and EAST current drive experiments need the fast RF waves to explain the observed electron X-ray spectrum. (EAST launches 3 GHz and Tore Supra/WEST

launches 5 GHz LHCD RF waves). The RF wave scattering broadens the fast electron distributions producing the observed X-ray spectrum and giving the larger core toroidal currents than those derived from the electrostatic LHCD RF codes [*Horton, et al. (2017)*] that neglect the coupling to the fast waves (DIII-D).

6.1.2 Electron Cyclotron Heating (ECH) for control of 3/2 and 2/1 magnetic islands and steady-state tokamak plasmas in DIII-D, EAST and KSTAR

DIII-D demonstrated the use of RF Doppler Backscattering (DBS) experiments for measuring the radial distribution of the resonant ECH driven electron heating and the associated modification or control of the toroidal plasma current [*Brookman, et al. (2017)*]. The ECH theory and modeling are essential for developing real-time control of the growth of magnetic islands at the $q(r) = 3/2$ and $2/1$ rational surfaces. Theoretical analysis of the RF code data from LUKE/C3P0 and GENRAY simulations for the experiments with six 110 GHz gyrotrons producing the Doppler Backscattering (DBS) database. With modeling of the “ B_t -jog” diagnostic technique [*Houshmandyar, et al. (2017)*], one is able to interpret the interplay of the ECH RF waves with the ETG turbulence.

Both DIII-D data and earlier data from Tokamak Fusion Test Reactor (TFTR) is analyzed to determine the required focusing and to estimate the total RF gyrotron powers needed to stop, or control, the growth of the magnetic islands. Without the RF control the island growth leads to plasma disruptions and events that lower the plasma Q_{DT} by significant factors. Near real-time RF ECH plasma control is now understood to be essential for steady tokamak operation.

6.1.3 Direct ∇T_e measurements with high spatial resolution of T_e -profiles using electron cyclotron emission

Electron Cyclotron Emission (ECE) diagnostics use Yttrium-Iron-Garnet (YIG) bandpass filters to measure with precision the electron temperature $T_e(r, t)$ profiles and their fluctuations δT_e . These (x, t) variable bandpass frequency filters were compared with fixed frequency filters and shown to give higher resolution electron temperature measurements. *Houshmandyar, et al. (2018)* present proof-of-principle for high temporal resolution measurements of the electron temperature gradient by using real-time slewing with a YIG bandpass filter for measuring the location of an ECE channel during a long pulse. The key instrument uses the application of YIG tunable filters with their narrow bandwidths and capability for a high slew rate of their center frequency. This instrument permits fast relocation of the ECE channels for direct measurement of the temperature gradients with close spacing of channels to study the dynamics of the magnetic islands.

ECE diagnostics are essential to tokamaks and all fusion machines. Employing narrow bandwidth bandpass filters in the Intermediate Frequency (IF) section of a radiometer ECE diagnos-

tic increases the spatial resolution of T_e -profile [Truong, *et al.* (2014)] and sensitivity for T_e -fluctuation (δT_e) [Fontana, *et al.* (2017)] measurements. Utilizing Yttrium-Iron-Garnet (YIG) bandpass filters reduces the threshold for the δT_e measurements. These instruments are critical for correlational ECE measurements for turbulent transport studies [Fontana, *et al.* (2018)]. The tunable feature of the YIG filters yields the flexibility for moving the ECE channels to different spatial regions during a single discharge. This is important in plasma control during the fast rearranging of the ECE channels to the moving rational surfaces. This diagnostic generates enough information for the actuators to control the Neoclassical Tearing Modes (NTM).

6.1.4 Impurity ion injection for controlling transport dynamics in tokamak plasmas

The JET ITER-Like Wall (JET-ILW) experiments [Lang, *et al.* (2013)] showed that predicting and control of the wall erosion and the inward transport of high- Z ions from the tungsten W wall coatings is critical for maintaining steady fusion power plasmas.

In order to obtain a better understanding of tungsten (W) transport processes, we are developing the Monte Carlo W transport code (IMPGYRO). The code has the following characteristics which are important for calculating the tungsten W transport: (1) the exact Larmor motion of W ions is computed so that the effects of orbital drifts are automatically taken into account; (2) Coulomb collisions between W impurities and background plasma ions are modeled using the Binary Collision Model which provides more precise kinetic calculations of the friction and thermal forces. By using the IMPGYRO code, the W ion production/transport in the ITER geometry is calculated under two different divertor operation modes (Case A: partially detached state and Case B: high recycling state) obtained from the SOLPS-ITER code suite calculations without the effect of drifts. The results of the W-density in the upstream Scrape-off Layer (SOL) strongly depends on the divertor operation mode. From the comparison of the W impurity transport between Case A and Case B, obtaining a partially-detached state is shown to be effective in reducing the W-impurities in the upstream SOL. The limitations of the model and the validity of the above results are discussed and summarized for further applications of IMPGYRO code to ITER plasmas [Yamamoto, *et al.* (2017)].

6.1.5 RF wave control of steady-state fusion plasmas

RF waves are an irreplaceable tool for plasma current-drive and for controlling plasma instabilities. RF research quantitatively predicts how the SOL turbulence and core turbulence scatter the RF waves leading to deposition profiles that strongly modify currents given by neoclassical and collisional transport models. This RF power leads to and couples directly to the wall erosion mechanisms through the development of plasma wall dust and impurity transport from the SOL through the magnetic separatrix into the core plasma. Elucidation of these critical processes brings

the tokamak fusion program closer to the predictive capability that are needed for interpreting the ITER plasma data. Impurity transport models [Hazeltime (2009)] and computer software are essential for the design of future fusion reactors.

6.1.6 Impurity transport from Tracer–Encapsulated Solid Pellets (TESPEL) experiment in LHD with impurity diagnostics

Experiments with additional strong auxiliary RF heating (ICH/ECH) have demonstrated the suppression and mitigation of the core impurity accumulation. The data is from the Tracer–Encapsulated Solid Pellet (TESPEL) experiments [Sudo, *et al.* (2012)] on the LHD and the impurity control experiments on the W7–AS Stellarator [Burhenn, *et al.* (2009)]. The Mn, Co, V injected tracer elements are between Fe, W and Cobalt elements used in metal plasma walls in the KSTAR [Hong, *et al.* (2015)] machine.

The TESPEL experiments on the LHD used tracer elements encapsulated in balls of polystyrene with Mn, Co, V impurities in the balls of 0.1 mm size are injected in to the plasma. Measuring with spectrometers the emitted radiation lines gives level and spatial distribution of the impurities. Other machines with impurity control experiments are the W7–AS Stellarator [Burhenn, *et al.* (2009)], and the Korea Superconducting Tokamak Advanced Research (KSTAR) tokamak [Hong, *et al.* (2015)].

In the KSTAR experiments [Hong, *et al.* (2015)] the addition of Electron Cyclotron RF Heating (ECH) of 1.5 MW 154 GHz ECH suppresses the impurity emission from the highly–ionized V tracer atoms. The LHD experiments show that high–power (1.5 MW) 154 GHz ECH can reduce the accumulation of the impurities. Optimum ECH conditions (Power, Absorbed Position and Duration) are used to control the impurity accumulation.

Experiments on DIII–D traced the anomalous radial distribution of the ECH power deposition by the RF scattering from the ambient plasma turbulence. Modeling for WEST steady–state RF operation yields contributions to the core current drive that were previously missed in modeling without the plasma turbulence. The critical steps include pitch–angle scattering of the RF rays from the drift wave density turbulence as modified by the anisotropic electron momentum distributions produced from the antenna–launched RF waves phase velocities ranging from $4v_e$ to one–half the speed of light. The modeling shows how the density fluctuations from the electron temperature gradient turbulence scatter the RF waves from the slow–wave polarization (quasi–electrostatic lower hybrid waves) into the fast wave or whistler RF waves [Horton, *et al.* (2017)]. This turbulence scattering is necessary to explain the measured core electron X–ray emissions. The LHCD research for WEST is reported in the RF Heating Conference Proceedings Aix en Provence, June 2017.

The plasma turbulence, due to the steep temperature gradients across the Last Closed Flux Surface (LCFS), is critical in scattering the RF waves. The wave–scattering calculations show how the plasma pressure gradients drive FLR–ballooning interchange instabilities producing pulses of vortices into the SOL edge plasma [Miura, *et al.* (2017, 2018)]. The anisotropies created in the

ion velocity distributions span from inside the last closed flux surfaces into the Scrape-Off Layer (SOL) creating (i) the inward radial electric fields, (ii) the ion pressure anisotropy (p_{\parallel}, p_{\perp}) and (iii) the sheared E_r fields that control the Hall-MHD turbulence and (iv) the creation of vortex structures or plasma “blobs”.

Research on the turbulence inside and outside the last closed flux surface is a focus for future research in ITER. Work on the RF-driven plasma structures will expand rapidly in the coming years with high priority for modeling steady-state fusion plasmas.

Tokamak/Stellarator vs. FRC: transport and other fundamentals (Y. Kishimoto and T. Tajima)

Plasma, highly-nonlinear medium consisting of ions and electrons, exhibits prominent characteristics, self-organization and structure formation, once several conditions are fulfilled. In some cases, they are expected and useful in achieving a purpose, while in some cases, accidental and eliminated. Fusion device, one of the promising plasma applications for future energy resource, is designed so as to minimize macro and microinstabilities in achieving high stability and confinement, so that the characteristics are of specific importance [Horton (1999)]. When we design a device, we usually rely on the linear aspect, while uncertain whether the characteristics, i.e. the self-organization and structure formation, support the approach or lead contradiction.

Tokamaks and stellarators have strong toroidal magnetic fields and additional magnetic field, i.e. poloidal magnetic field, by plasma current in tokamaks and by external coil in stellarators, so that the latter is more rigid than the former, which possess more freedom in magnetic configuration. Such magnetic structures are designed to have magnetic shear in minimizing various instabilities from the linear aspect while it is found to induce the overlap of drift wave “islands” called streamers, i.e. global modes, and causes avalanche-like intermittent bursts leading to self-organized critical transport [Kishimoto, *et al.* (1996)]. This is peculiar to so called L-mode that causes anomalous ion/electron diffusion known as the Bohm transport. A recipe to prevent such anomalous diffusion is to weaken and/or eliminate the magnetic shear by the reversal of magnetic shear or by the annihilation of streamers by the additional electric field generated shear, which leads to high confinement state, e.g. internal transport barrier.

We compare and understand that the presence of null magnetic shear in stellarator enhances its confinement, much the similar way to the above tokamak’s local shearlessness contributing to the enhanced confinement [Ishizawa, *et al.* (2016)]. Namely, through the series of research on fusion devices with strong and then rigid guiding magnetic field, we found a reciprocal relation between linear stability and nonlinear turbulent transport as that the configuration with more unstable smaller magnetic shear plasma provides smaller turbulent transport nonlinearly than that with moderate shear. This suggests that softening the (“rigidness” of the system is of importance for the plasma to be self-organized in keeping higher stability and confinement.

From this viewpoint, high-energy beam assisted FRC [Binderbauer, *et al.* (2015)] is charming system. FRC is devoid of strong shell-like fields and thus is bound to be wobbly. First, the FRC

core is devoid of magnetic shear (an agent of the radial extended transport channels). Secondly, the core is devoid of the instability driving mechanism of drift wave due to the Finite Larmor Radius (FLR), short electron connection length, and reversed $\nabla - B$ drift. However, the beam-driven FRC has an entirely additional dimension. The beam introduces the backbone to the overall plasma that makes FRC globally stable, while enhanced FLR due to the beam further solidifies the FRC stability. The additional but not yet well-known robustness of the beam-FRC combo is the principle that the beam-induced waves with high phase velocity cannot destroy the plasma confinement, just similar to the intense wake field not destroying the plasma accelerator. We are planning to check this point by our gyrokinetic code of FRC.

6.1.7 Reduction of edge plasma turbulence via cross-phase coherence decrease by zonal fields

Transport of the near-adiabatic plasma is readily and widely simulated numerically. The Zonal Flow (ZF) along the poloidal direction is found to emerge self-consistently from the turbulence. Zonal flow $V(n)$ fields are found to feed back to turbulence by reducing the cross phase. As a result, the turbulence is localized with depressed peaks. Turbulence is low and the cross phase δ is negative near $V = 0$, where the gradient V' (vorticity) of the ZF along the radial direction is large. The fluctuations are almost localized where the zonal-density gradient \bar{n}' is a positive peak and V is locally large. Positive \bar{n}' or positive $V'S$ is shown to reduce the cross phase between the electric potential and the density fluctuation [Kim, *et al.* (2019)].

Action principles for extended magnetohydrodynamic models

The general, nondissipative, two-fluid model in plasma physics is Hamiltonian, but this property is sometimes lost or obscured in the process of deriving simplified (or reduced) two-fluid or one-fluid models from the plasma fluid equations of motion. To ensure that the reduced models have a Hamiltonian structure, Charidakos, *et al.* (2014) start with the general two-fluid ion and electron action functional, and make all the approximations, changes of variables, and expansions directly within the action variables context. The resulting equations are then mapped to the Eulerian fluid variables using a novel nonlocal Lagrange-Euler map. Using this method, the Lüst (1960) general two-fluid model, the extended Magnetohydrodynamic (MHD), the Hall-MHD, and the electron MHD model are all derived from a unified theoretical framework. The variational formulation allows the application of the Noether's theorem to derive conserved quantities for each action symmetry of the plasma dynamics.

Extended magnetohydrodynamics is required in many plasma machines. A hollow cathode is the electronic source and neutralizer of the Hall thruster and an ion thruster. When the orbit of an all-electric propulsion satellite changes from 100 km to 36000 km, the back-pressure changes by two to three orders of magnitude. The influence of the back-pressure on the discharge characteristics

of the hollow cathode has been studied experimentally in the so-called diode configuration. With the increase in the back pressure, the anode voltage decreases gradually, and the amplitude of the current oscillation decreases significantly. Additionally, the plasma is relatively stable, the most probable ion energy and the width of the ion energy distribution reduces, and the electron distribution function inclines toward the Maxwell distribution under high back pressure. The analysis results show that the back pressure affects the gas ionization and the ionic acoustic turbulence, which also affects the discharge characteristics of the hollow cathode [Ning, *et al.* (2018)].

6.1.8 Creation of plasma “blobs” outside the magnetic separatrix

Theory for the formation and dynamics of the plasma “blobs” opens up the possibility that the SOL plasma profiles can be predicted with greater accuracy. Research on the smaller laboratory machines, including the Helimak and Large Plasma Device (LAPD), indicates that plasma blob filaments contribute to, and in some cases, dominate the plasma profiles. Erosion at the vessel walls competes with emission at the divertor wall in determining the impurity contamination in the plasmas. The SOL plasma plays an important role in impurity erosion and thus the total impurity content of the core plasma. The Breizman, *et al.* (2018) analysis of plasma input shows that during an inductive start-up, there develops a nonmonotonic distribution function in parallel momentum for a group of electrons that are continuously accelerated. The energy gain of these runaway electrons is limited by a combined effect of pitch-angle scattering and synchrotron radiation. The result is a radial transport with high-energy electrons escaping through the magnetic separatrix. This scenario is qualitatively confirmed by the ohmic plasma data in both JET and Tore Supra [Fontanilla and Breizman (2017), Breizman and Aleynikov (2017)].

6.1.9 Convective transport by intermittent blob-filaments

A plasma blob-filament (or simply a “blob”) is a localized magnetic field-aligned plasma vortex structure that is considerably denser than the surrounding background plasma and localized in the directions perpendicular to the equilibrium magnetic field B . In experiments and simulations, these intermittent filaments are often formed near the boundary between open and closed field lines, and seem to arise in theory from the saturation process for the turbulence edge instabilities. Blobs become charge-polarized under the action of an external force which causes unequal drifts on ions and electrons; the resulting polarization-induced $\mathbf{E} \times \mathbf{B}$ drifts move the vortices radially outwards across magnetic separatrix into the Scrape-Off Layer (SOL) plasma of toroidal and in mirror machines (CLM) plasmas.

The blob transport is a general phenomenon occurring in nearly all plasmas outside the closed magnetic flux surfaces. D’Ippolito, *et al.* (2011) review the relationship between the experimental and theoretical results on blob formation, dynamics and transport and assesses the degree to

which blob theory and simulations can be compared and validated against experiments. There are numerous publications on the dynamics of the vortices and blobs in the SOL plasma.

A profile for the critical temperature gradient scale length [$L_{T_e}^{-1} = -\nabla T_e/T_e$] was extensively measured in L-mode discharges in the Alcator C-Mod tokamak, where electrons were heated by ICRF waves through the minority heating method that produces changes by simultaneously varying heat fluxes and the local temperature gradients. The electron temperature gradient scale length profile was measured via the B_T -jog technique [Houshmandyar, *et al.* (2016)] and compared with electron heat flux from power balance analysis using TRANSP. The T_e profiles were shown to be stiff and already at the critical gradient values. The measured $L_{T_e, \text{crit}}$ profile is in agreement with ETG turbulence models which predict the dependence of q/L_{crit} on the local $Z_{\text{eff}}, T_e/T_i$, and the ratio of the magnetic shear to the safety factor s/q . The GENE gyrokinetic simulations confirm that the ETG is the dominant mode of turbulence in the electron scale ($k_{\perp} \rho_s \gg 1$). The gradient-turbulence data results agree with results first shown for LHCD-driven $T_e(r, t)$ profiles in Tore Supra in Horton, *et al.* (2000) and Hoang, *et al.* (2003). The results for WEST were subsequently developed in Horton, *et al.* (2017).

An in-depth understanding of the collective modes that can be excited in a wide range of high energy plasmas is necessary to advance nuclear fusion research in parallel with other fields that include space and astrophysics in particular. Important achievements are shown to have resulted from implementing programs based on this reality, maintaining a tight connection with different areas of investigations. This involves the undertaking of a plurality of experimental approaches aimed at understanding the physics of fusion burning plasmas. At present, the most advanced among these is the Ignitor experiment involving international cooperation, that is designed to investigate burning plasma regimes near ignition for the first time [Coppi (2015)].

A profile analysis of the L-mode plasmas near the critical electron temperature gradient scale length L_{crit} in the Alto Campo Toro (Alcator C-Mod) tokamak is carried out where the electrons were heated by an ion cyclotron range of frequency through a minority-heating method. The analysis was simultaneously varying the heat flux and that continuously changes the local temperature profiles and their gradient scale lengths. The electron temperature gradient scale length L_{T_e} profile was measured via a B_T -jog technique [Houshmandyar, *et al.* (2016)] and was compared with electron heat flux measured T_e profiles with a power balance Transport (TRANSP) analysis. The T_e profiles were shown to be stiff and already above the critical gradient values. The profile stiffness was found to be reduced near the $q = 1/4$ and $3/2$ surface. The measured critical scale length L_c from the $T_e(r)$ profile is shown to be in agreement with Electron Temperature Gradient (ETG) model which predict the dependence of L_c^1 critical scale length on the dependent on the local $Z_{\text{eff}}, T_e/T_i$, and the ratio of the magnetic shear to the safety factor. The results from linear Gyrokinetic Electromagnetic Numerical Experiment (GENE) simulations suggest ETG is the dominant mode of turbulence in the electron scale ($k \rho_s > 1$), and ion temperature gradient/trapped electron mode modes in the ion scale ($k \rho_s < 1$). The measured gradient length L_c profile is in agreement with the profile of ETG critical gradients deduced from GENE simulations. [AIP Publishing (<https://doi.org/10.1063/1.5022180>).

6.1.10 Enhanced confinement properties in H-mode and super-H shots

Fusion power requires one to maintain the burning plasmas with confinement properties significantly improved over those observed in auxiliary-heated L-mode tokamak discharges in order to achieve the key objectives of fusion plasmas. Thus, we understand the importance of the physics responsible for the favorable trends exhibited, for example, by supershot discharges in TFTR and by the H-mode-type divertor-controlled plasmas. In addressing this general issue, *Tang, et al.* (1989) reports results of theoretical investigations dealing with the onset conditions of the microinstabilities strongly influencing the plasma confinement behavior with gyrokinetic particle simulations interpreted with analytic models for the saturation and transport properties of these instabilities. Comparisons of experimental results with predictions from turbulent transport codes using microinstability-based theoretical formulas for particle, momentum, and energy fluxes must agree with the plasma data.

The theoretical and numerical studies on kinetic microinstabilities, including Ion Temperature Gradient (ITG) driven modes, Trapped Electron Modes (TEMs) in the presence of impurity ions as well as impurity modes (IMs), induced by impurity density gradients, in toroidal magnetized plasmas, such as tokamak and the Reversed-Field Pinch (RFP) are reviewed. The basic theory for IMs, the electrostatic instabilities in tokamak and RFP plasmas, are well developed. The observations of hybrid and coexistence of the instabilities are categorized systematically. The effects of impurity ions on electromagnetic instabilities such as ITG modes, the Kinetic Ballooning Modes (KBMs) and kinetic shear Alfvén modes induced by impurity ions in tokamak plasmas of finite- β ($=$ plasma pressure/magnetic pressure) are important.

Microinstabilities, such as Ion Temperature Gradient (ITG) driven modes and Trapped Electron Modes (TEMs), are widely accepted to be responsible for the anomaly of cross field particle, momentum and energy transports, observed experimentally in magnetic confinement fusion plasmas, and have been under intensive investigation in recent decades [*Horton* (1999), *Tang* (1978), *Liewer* (1985), *Doyle* (2007)]. On the other hand, it is well recognized that (nonhydrogenic) impurity ions are inevitable in toroidal fusion plasmas, owing to unavoidable interactions between plasma and plasma-facing materials such as vacuum vessel and divertor plates. The impurity ions have significant effects on plasma confinement via radiation loss of energy and the dilution of main fusion ion density. In addition, impurity transport, induced by neoclassical mechanism and turbulence, is important. In particular, turbulent impurity transport, induced by ITG and TEM instabilities, has been studied theoretically and experimentally, and significant progress has been achieved [*Moradi, et al.* (2011, 2012), *Angioni and Peeters* (2006), *Angioni, et al.* (2017a,b), *Fülöp and Nordman* (2009), *Wade, et al.* (2000), *Sertoli, et al.* (2011, 2015), *Futatani, et al.* (2010)]. The isotope effects of the instabilities and transport in the presence of impurity ions have also been investigated by *Dong, et al.* (1994), *Shen, et al.* (2016a,b), *Guo, et al.* (2017). Impurity effects on residual zonal flow in deuterium-tritium plasmas has been studied [*Guo, et al.* (2017)].

6.1.11 Isotope effects on plasma turbulence

Isotope effects on instabilities driven by Ion Temperature Gradient (ITG) and impurities in tokamak plasmas in the presence of tungsten ions are numerically studied [Shen, *et al.* (2018)]. It is revealed that the tungsten ions significantly modify the isotope scaling of the maximum growth rates of the instabilities with respect to the main or effective ion mass number M_i or $M_{\text{eff}} [= (1 - f_z)M_i + f_z M_z]$ with $f_z (= Z n_z / n_e)$ being impurity charge concentration. The most reasonable scaling is deduced as $\gamma_{\text{max}} = M_{\text{eff}}^{-15 \pm \beta}$ with $\beta \sim 0.8$, for ITG-driven modes, while $\gamma_{\text{max}} = M_i^{-0.4 \pm \beta_1} Z_{\text{eff}}^{12 \pm \beta_2}$ holds with $\beta_1 \sim 0.2$, $\beta_2 \sim 0.4$ for tungsten impurity modes, in significant contrast with the case of light or intermediate impurities where the scaling is $\gamma_{\text{max}} = M_{\text{eff}}^{-0.5}$ and $\gamma_{\text{max}} = M_i^{-0.5} Z_{\text{eff}}^{1.5}$ for ITG and impurity modes, respectively. These results suggest that existence of tungsten impurity would enhance (weaken) the isotope effect of instability driven by ITG (tungsten impurity ions), which is beneficial (harmful) for improvement of confinement when hydrogen isotopes are used in plasmas. The results might also provide hints on studies of particle and energy transports and discharge performance, particularly, in ITER-like wall machines.

The analysis of the influx of impurities from the confinement vessel walls called the “plasma-facing components” is described in detail by Casson, *et al.* (2015).

The WEST and the EAST tokamaks create quasi-steady-state high-temperature plasmas that have plasma dust particles from their beryllium, molybdenum and tungsten wall components simulations of the dust transport of these elements explains the observed light emission data. There are experiments in the Magnetized Dusty Plasma Experiments (MDPX) at Auburn University that provide a test bed for dusty plasma transport theory and simulations. The transport of impurities into fusion-grade plasmas with numerous earlier publications on impurity ion transport starting with the TEXT transport experiments [Horton and Rowan (1994)].

6.1.12 Dust particles in edge plasmas

Dust particles emitted from the plasma-wall interactions modify the drift waves in the plasma scrape-off layer which then causes some dust particles to gain sufficient energy to be injected through the magnetic separatrix into the core plasma. The plasma in contact to the vessel walls produces evaporation and the ejection of ions from the wall into the scrape-off layer plasma. The ions ejected from the walls are often in clumps of about 500 nm to 1 micron in size and are called plasma dust particles. These dust particles collect electrons, become negatively charged and gain energy from the electric fields in the edge or Scrape-Off Layer (SOL) plasma. Some of the dust particles are accelerated to high energies and cross the magnetic separatrix into the core plasma.

The dust particles are continuously undergoing a change in their charge $Z_d e$ due to the interaction with the ionized plasma. The dust particles become highly charged with $Z_d = 10^3$ to 10^4 with a radius a of the space dust particle much less than the Debye length. The radius a of the dust particles range from of order 10 nm to 1 micron (= 1000 microns). The charging rate is

dZ_d/dt is a function of the electron and ion thermal velocities and the parameter

$$Z = \frac{Z_d e^2}{a T_e}. \quad (6.1)$$

With the balance for steady state occurring when $Z(t)$ reaches the value

$$\frac{\omega_{pe}^2}{v_{T_e}} = \frac{\omega_{pi}^2}{v_{T_i}} \frac{T_i}{T_e + Z}. \quad (6.2)$$

For $m_i/m_e = 1836$ and $T_e = T_i$, the charge balance occurs with $Z = 2.5$ [Benkadda, *et al.* (1995)]. When the charging rate reaches steady state $dI(Z_d)/dt = 0$. The charging rate is approximately given by

$$\frac{d\delta Z_d}{dt} = -\nu/\chi \delta Z_d \quad (6.3)$$

where the rate is given by

$$\nu\chi = \omega_{pi}^2 d \frac{(1 + \tau + Z)}{\sqrt{(2\pi v_i)}}. \quad (6.4)$$

6.1.13 Advances in modeling of plasma pedestal behavior and Edge Localized Modes (ELM) control in ITER reference plasma scenarios

Progress in the modeling of the edge–pedestal plasma behavior in ITER plasmas including linear and nonlinear MHD stability analysis, ELM triggering by pellet injection and vertical plasma oscillations and ELM control by the application of 3D fields is described. These activities are implemented under the framework of ITER Scientist Fellow Network Pedestal Group to improve the understanding of the physics processes that dominate ITER pedestal plasmas thus providing a firmer physics base to evaluate the edge plasma properties in ITER H–mode plasmas and for the physics–based extrapolation of results obtained in present experiments to ITER [Loarte, *et al.* (2018)].

The experimental campaigns of (2016-02019) on JET resulted in a simultaneous extension of density and confinement in ELMy H–mode plasmas using various methods. By further increasing the average triangularity of the plasma, discharges have now been realized with values for $H_{98(y,2)} \geq 1$ and $n/n_{GW} \sim 1.1$, which exceeds what is required for the ITER $Q = 10$ standard scenario discovered on JET. The flat–top duration of these discharges is about 5s and is only limited by technical constraints on JET. These high–density, high–confinement discharges exhibit energy losses by other mechanisms than pure ELM activity which points to a possible way of ELM mitigation. High density in high– δ discharges leads to a reduction in the ELM frequency, which is in contrast to the usual relation between ELM frequency and ELM size.

Detailed analysis of the ELM behavior and additional thermographic measurements on the

divertor targets indicate that there is a window for operation for Type I ELM discharges in ITER. Impurity seeding is an additional tool to mitigate ELMs in discharges with high and low triangularity and has no detrimental effect on energy confinement or neutron production. Pellet injection from the high-field side with a tailored injection rate has produced discharges with high density and high confinement, but more work is needed to optimize the stationarity. Discharges with strong density peaking ($n(0)/n_{\text{ped}} \sim 2$) have been obtained without pellet injection, by careful gas dosing over long time intervals. Density peaking and high- β values both favor the destabilization of NTMs due to the associated increased bootstrap current fraction. This can be a limiting factor for the confinement properties of such plasmas, unless care is taken to avoid the creation of large seed islands, induced by large first ELMs or sawteeth, or by varying the ICRH phasing. Confinement studies show an increase of energy confinement with density peaking and triangularity, but still there is a degradation of confinement with increasing Greenwald factor. Density peaking and plasma shaping have a beneficial influence on confinement. Confinement scaling studies with data from He discharges confirmed the mass dependence of the IPB98(y, 2) scaling, and combined with previous T and H studies, suggest $\tau_E \propto M^{0.19} Z^{-0.59}$. Threshold power studies in He show the same dependence on magnetic field, density and mass as for deuterium, but the absolute value is about 50% higher in He. Extensions of the results to higher currents, fields and heating powers and towards longer flat-top durations on JET are being prepared for ITER. Plasma configurations at high average triangularity have been developed, reducing the disruptive forces of the ITER-like configuration, allowing plasma operation at JET up to 4 MA/4 T, in order to study the performance at higher absolute densities and operation closer to ρ_*^{ITER} . Such plasmas require at least 25 MW of additional heating power to reach the H-mode.

Various diagnostics have been enhanced to increase the diagnostic capabilities of JET. A inboard pellet track aiming more centrally and allowing higher pellet speeds was installed to further optimize plasma fueling by high-field side pellet injection. Long-pulse scenarios were prepared with a divertor phase of over 50 s and with potential for further extensions well over 1 min, giving a new tool for studies on the stationarity of various plasma parameters and of recycling during long-time intervals.

With its divertor configuration, plasma size, heating, current drive and diagnostic systems, tritium, beryllium and remote-handling capabilities, the JET device accesses a wide range of operating regimes in experimental conditions close to those of a burning plasma experiment. Prior to and during the design phase of ITER, JET produced major contributions to the ITER physics basis [*ITER Physics Basis* (1999)] used to extrapolate plasma performance to ITER. The JET research program has focused on issues critical to finalizing the details of the ITER design.

6.1.14 High-pressure relaxed-plasma confinement

High-pressure plasmas with reversed magnetic fields and nonuniform rotational flows are ubiquitous in nature and are produced in Field-Reversed Confinement (FRC) laboratory plasmas [*Schmitz, et al.* (2016)]. A large toroidal plasma current driven by neutral beam injection and external magnetic field driven by poloidal field coils produce the confinement geometry.

The Grad-Shafranov equilibria [Copenhaver (1983), Cerfon and Freidberg (2010)] describe cylindrical magnetic fields from external field coils and toroidal plasma currents [Schmitz, *et al.* (2014, 2016)]. We describe the ion and electron orbits in the geometry of the Norman FRC machine with 12 external coils and the plasma current. Ions are launched from 8 NBI injectors at 35 KeV for 100 msec producing a $T_i \sim 2\text{--}3\text{ KeV}$ and $T_e \sim 500\text{ eV}$ plasma. There is sheared $\mathbf{E} \times \mathbf{B}$ flow across the outer closed magnetic field lines. The ion orbits become chaotic in the mirroring region where the radius of curvature is comparable to ion gyroradius. There are ion orbits called the “butterfly pitch angle” distributions measured in the magnetosphere and chaotic orbits [Shibahara, *et al.* (2010)]. These orbits affect the drift waves and the Alfvén wave stabilization. Analytic theory and 3D computer simulations are used to interpret the results of the measured plasma. A strong radial electric field $E_r(r, t)$ develops $\mathbf{E} \times \mathbf{B}$ sheared rotation that suppresses the core turbulence.

Turbulence in the scrape-off layer plasma is modified by the nonlinear transverse cascade. The $p \sim B^2/2\mu_0$ plasma is in a relaxed self-organized state. The turbulence is compared with the density fluctuations measured from X- and O-mode RF wave field scattering data [Schmitz, *et al.* (2016)].

In space physics the generation mechanism of a butterfly Pitch-Angle Distribution (PAD) of energetic ions is demonstrated by test particle simulations in the stretched magnetic field [Shibahara, *et al.* (2010)]. Polar satellites detect some events from the butterfly PADs of the energetic protons $\gtrsim 80\text{ KeV}$ in the outer ring current region around midnight near the equatorial plane. They were observed at a relatively disturbed time in the inner magnetosphere and the ring current is developed; that is, where the magnitude of the magnetic field at the Polar satellite was highly depressed and the adiabaticity of the protons were expected to be violated. To reproduce the butterfly pitch-angle distribution, a test particle simulation in which the first adiabatic invariant μ can be monitored are performed. When the radius of the field line becomes comparable to the Larmor radius of a proton, the protons have significant scattering of pitch angle (α) due to change of μ . This μ -scattering process reforms the PADs. Owing to cumulative μ -scattering, the flux of the protons have a peak at $\alpha \sim 40^\circ$ (or 140°) and collapses at $\alpha \sim 0^\circ$ (or 180°) and 90° , which produces butterfly PAD distribution. The computed PAD resembles the butterfly PADs observed by the Polar satellite [Shibahara, *et al.* (2010)]. The nonadiabatic effect is important for not only the generation mechanisms of the butterfly PAD but also for the development of the storm-time ring current.

In the 2004 shutdown, a new in-port ICRF antenna was installed on JET with the aim to validate key elements of the ITER-ICRF design. JET diagnostic upgrades included a Charge Exchange Recombination Spectroscopy (CXRS) core and edge, magnetics, bolometry, neutron spectrometry, microwave waveguides and divertor diagnostics. New diagnostics included a high-resolution TS system, TAE active antenna system, wide-angle infrared view, halo sensors, lost α particle detectors and a comprehensive system of erosion/re-deposition diagnostics.

JET continues to provide contributions to our understanding of tokamak physics, scaling predictions for ITER, further development of ITER operating scenarios and testing of ITER relevant systems such as heating and current drive, diagnostics and tritium technologies.

The impact of an initial random magnetic field disturbance on the temporal evolution of a two-dimensional incompressible turbulent shearless mixing layer is investigated using direct

numerical simulation. Different intensities of the initial random magnetic field are imposed with uniform probability distribution on an identical flow field. The initial flow-field condition is the turbulent shearless mixing layer with different kinetic energy ratios and identical integral length scales. Simulations are carried out in a moderate magnetic Reynolds number, which causes a two-way interaction between the velocity and magnetic fields. In order to analyze the effect of the initial random magnetic field on the mixing characteristics, the intermittency inside the mixing layer and the mixing evolution parameters are investigated. With small initial magnetic field intensity, the intermittency occurs in both large and small scales compared to those in hydrodynamic flows. However, increasing the intensity of the initial magnetic field reduces the intermittency in the mixing region to lower values compared to the hydrodynamic flow. The mixing layer growth rate and the mixing efficiency both show reduction by increasing the initial magnetic field intensity, which is attributed to the reduction of the averaged Reynolds number of both homogeneous isotropic turbulent regions due to the suppressing effect of the Lorentz force on the velocity fields of these regions.

Plasma response to three-dimensional Resonant Magnetic Perturbations (RMP), applied for the purpose of controlling type-I Edge Localized Modes (ELMs) in ITER with the baseline ELM control coils, is computed using a toroidal, resistive, full magnetohydrodynamic model. Considered are five representative ITER plasmas, designed for different phases of the ITER exploration. The plasma response, measured by the plasma boundary corrugation, is found to be similar for the two DT scenarios at full plasma current (15 MA) and full toroidal field (5.3 T) but different fusion gain factors ($Q = 5$ versus $Q = 10$), indicating similar ELM control performance with the same RMP coil current configuration.

The other plasma scenarios, with proportionally scaled down plasma current and toroidal field, can have different plasma boundary corrugation. The key plasma parameter affecting the response is the plasma toroidal flow near the pedestal region, which significantly varies depending on the transport model assumption for the toroidal momentum. Lower pedestal flow leads to a stronger edge peeling response from the plasma and thus a better ELM control. The optimal coil configuration for controlling type-I ELMs is similar for all four ITER plasmas with similar safety factor but different current levels, but is significantly different for the case at half plasma current (7.5 MA) and full field (5.3 T). On the other hand, for the purpose of controlling the radial profile of the plasma toroidal rotation in ITER using 3D fields, the relative amplitude of the toroidal torque density, between the plasma core and edge region, is optimized. Generally, a strong coupling between the core and edge torques is observed, largely due to the middle row of the ELM control coils. The best decoupling scheme of the core-edge torque distribution is to de-emphasize the role of the middle row coils. Optimal coil current configurations are found for the ITER 15 MA/5.3 T with $Q = 10$ plasma, that synergistically maximize the plasma edge-peeling response (indication for good ELM control) and the toroidal torque near the plasma edge (good for RMP field penetration through pedestal) [Li, *et al.* (2019)].

The effect of Resonant Magnetic Perturbation (RMP) on boundary turbulence and transport in J-TEXT plasma was experimentally investigated. Edge plasma fluctuations in discharges with and without the ($m/n = 3/1$) RMP currents are diagnosed by using Langmuir probe arrays and that fluctuations in the edge and Scrape-Off Layer (SOL) regions decrease with the application of

a 6 kA RMP. The broadband turbulence at the radial location of $\rho \sim 0.9$ which has a characteristic frequency of 40-150 kHz was strongly suppressed when applying RMP, as was the radial turbulent particle flux and blob transport in the near-SOL region. These experimental findings make RMP a promising method of suppressing and controlling turbulence and particle transport in a plasma boundary [Wu, *et al.* (2019)].

The ITER Scientist Fellow Network Pedestal Group has made significant progress in understanding of the physics processes that determine pedestal plasma behavior in ITER plasmas, their MHD stability and instability leading to ELMs as well as of ELM control has taken place by the modeling activities implemented under. New nonlinear MHD simulations show that ITER pedestal plasmas have the required characteristics to access the Quiescent H-mode (QH-mode) regime without ELMs by destabilization and saturation of low- n kink-peeling modes, although it is not yet clear if the rotational shear required to stabilize higher- n ballooning modes can be provided by the joint application of the NBI torque and the breaking torque provided by 3D fields from the in-vessel ELM control coils. Controlled ELM triggering has been further assessed for two schemes: pellet injection and vertical plasma position oscillations. For pellet triggering, it has been found that the proximity of the pedestal pressure to MHD stability limits plays an important role in determining the pellet size required to trigger an ELM (which is favorable regarding the optimization of plasma performance and minimizing fuel throughput for ELM control).

The required pellet sizes to trigger ELMs at lower plasma currents are much lower than for 15 MA plasmas, particularly at high q_{95} . This ensures that this scheme can be explored in the initial H-mode operational phases of the ITER Research Plan at lower plasma currents so that a decision can be taken regarding its applicability for high Q/I_p operation in ITER, which may require an upgrade of the pellet injection system from 4 to 6 injectors. Regarding vertical plasma oscillations, the nonlinear MHD simulations have given the physics basis to evaluate this scheme for ELM control in ITER and confirmed that pellet injection (tungsten ion W) can be used for currents up to 7.5 MA as backup when the other ITER ELM control schemes (ELM control by 3D fields and by pellet pacing) are being developed and tested.

6.2 High Magnetic Field Toroidal Fusion Machines

The IGNITOR Program maintains the objective of approaching D-T ignition conditions by incorporating systematically advances in relevant high magnetic field technology and in experiments on high density well-confined plasmas.

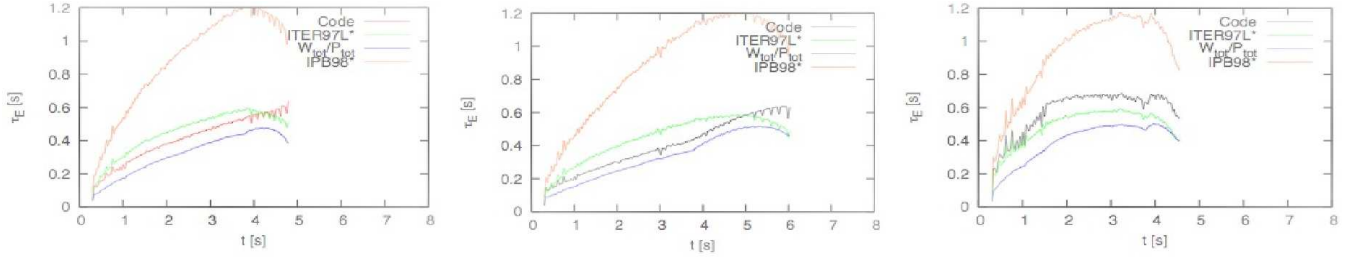


Figure 6.3: Evolution of the energy confinement time evaluated by the JETTO code $t_E = W_{tot}/P_{tot}^*$, compared to those given by the scalings ITER97L and IPB98, where $P_{tot}^* = P_W + P_a + P_{aux} - dW_{tot}/dt$. The adopted thermal energy transport models involve respectively, the so-called Coppi–Mazzucato, Bohm–gyroBohm, and Coppi–Tang transport coefficients.

Another objective is to chart the development of the high-magnetic field experiments. Considering that a detailed machine design has been carried out [Coppi, *et al.* (2013)], the advances made in different areas of the physics and technology that are relevant to the IGNITOR project are (i) Main Components Issues, Assembly and Welding Procedures; (ii) Robotics Criteria; Non-linear Feedback Control Simulations with 3D Structures and Disruption Studies; (iii) ICRH and Dedicated Diagnostics Systems; (iv) Anomalous Transport Processes Including Self-organization for Fusion Burning Regimes and Zero-Dimensional Model; (v) Tri-dimensional Structures of the Thermonuclear Instability and Control by ICRH Heating; (vi) Superconducting Components of the Machine and the Envisioned High-Field Superconducting Experiments.

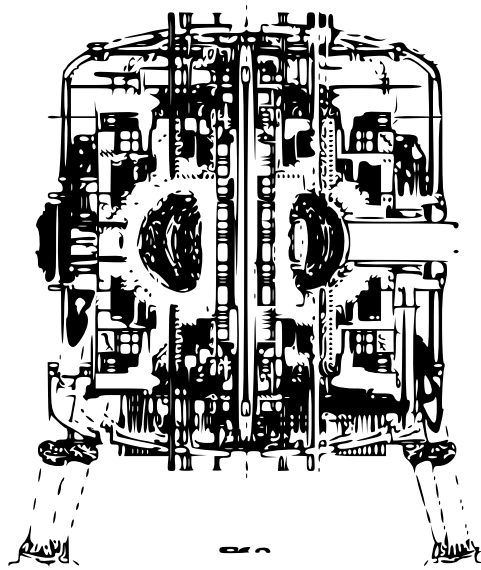


Figure 6.4: Vertical cross-section of the IGNITOR machine as presently designed.

The main objective of the IGNITOR Program is to explore the ignition conditions of magnetically confined D–T plasmas while producing significant amounts of fusion power up to about

100 MW. For this, a compact, high-field device has been designed that advances the line of high-field experiments which began with the Alcator program at MIT and was later also developed in Italy with the FT program. A relatively short but complete description and analysis of the machine core (see Figs. 6.11 and 6.12) has been given in *Coppi, et al.* (2013).

A detailed design of all the main machine components has been carried out and its results and drawings are now ready to be transferred to the industrial groups that have been identified as capable of constructing all the components of the machine core. The IGNITOR facility is expected to be operated at the Troitsk site of Rosatom and managed by the IGNIR collaboration between Italy and Russia. At this time the IGNITOR Program is the only one that has retained the objective of investigating this approach and the access to ignition conditions thanks to the regular updates of the machine design that have followed relevant advances in physics, technology and materials. The main machine parameters are included in Table 6.1 [*Coppi, et al.* (2013)].

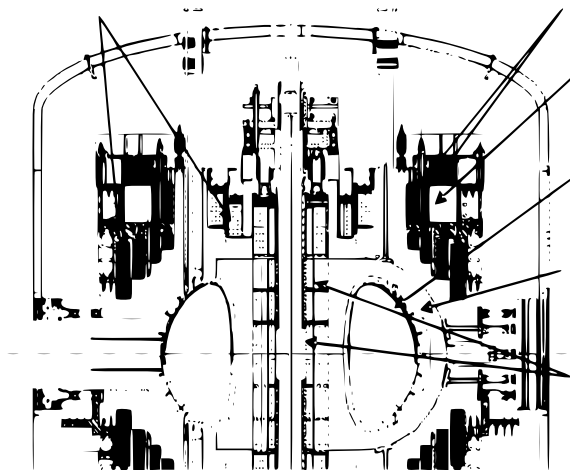


Figure 6.5: Sketch of the vertical cross-section of the IGNITOR machine where the main components are indicated.

Table 6.1: Example of Plasma Parameters [*Coppi, et al. (2013)*] for an 11 MA Operational Scenario from the JETTO Code

Toroidal plasma current I_p (MA)	11
Toroidal field B_T (T)	13
Major radius R_0 (m)	1.32
Minor radius $a \times b$ (m) ²)	0.47×0.86
Elongation k	1.83
Triangularity δ	0.4
Plasma volume V_9 (m ³)	10
Central electron temperature T_{e0} (KeV)	11.5
Central ion temperature T_{i0} (KeV)	10.5
Central electron density n_{e0} (m ⁻³)	9.5×10^{20}
Average electron density $\langle n_e \rangle$ (m ⁻³)	4.8×10^{20}
Central plasma pressure p_0 (MPa)	3.3
Alpha density parameter n_α^* (m ⁻³)	1.2×10^{18}
Average alpha density $\langle n_\alpha \rangle$ (m ⁻³)	1.1×10^{17}
Fusion alpha power P_α (MW)	19.2
Plasma stored energy W (MJ)	11.9
OH power P_{OH} (MW)	11.2
ICRF power P_{ICRH} (MW)	0
Bremsstrahlung power loss P_{brem} (MW)	3.9
Poloidal beta $\langle \beta_p \rangle$	0.20
Toroidal beta $\langle \beta_T \rangle$ (%)	1.2
Edge safety factor $q\psi = q\psi(a)$	3.5
Bootstrap current I_{bs} (MA)	0.86
Poloidal plasma current (MA)	$\cong 8.4$
Energy confinement time $\tau_{\alpha, sd}$ (S)	0.05

A major effort in the machine design has been that of producing a plasma column in which a high mean poloidal field $\overline{B}_p \simeq \sqrt{10}$ T can be reached together with plasma currents $I_p \simeq 10$ -11 MA while maintaining reasonable safety factors against the onset of macroscopic instabilities (i.e. $q(\psi_a) \simeq 3.6$). The rough arguments for this choice of objectives are as follows: High values of the confinement parameter $n\tau_E$, n being the particle density and τ_E the energy replacement time, should be reached considering that the maximum particle density should be related to the average current density $\langle J_\parallel \rangle \sim \overline{B}_p / \overline{a}$, where \overline{a} is the mean plasma minor radius, and that the confinement time should have a significant dependence on I_p . Then the maximum values of $n\tau_E$ should be related to \overline{B}_p^2 as $I_p \simeq 5\overline{a}\overline{B}_p$. Moreover, if we consider the mean plasma pressure to be limited by the magnetic pressure $\overline{B}_p^2 / (2\mu_0)$, the plasma reactivity represented by $n^2 \langle \sigma_f v \rangle \propto n^2 T^2$ can be expected to be related to \overline{B}_p^4 . These considerations have in fact been supported by sophisticated numerical simulations that have been carried out by 1+1/2D transport codes [*Coppi, et al. (2010, 2013)*, *Airolidi and Cenacchi (1997)*]. In this connection we observe that well-confined plasmas

with maximum densities close to 10^{21} m^{-3} have been obtained repeatedly by the Alcator line of experiments and, with lower temperatures, by the Large Helical Device machine. To facilitate the attainment of these densities, the adoption, as in the case of the Alcator C experiments, of a pellet injector is planned. In the case of IGNITOR, however, the required pellet speeds are considerably higher and further advances (expected to be possible) in the technology of these injectors are needed.

An important additional criterion that has driven the IGNITOR design process is that of having a strong Ohmic heating that would persist up to temperatures where α -particle heating can take over. Thus the need for an auxiliary heating system (ICRH is the only feasible option) is minimized together with the deterioration of the energy confinement time that has to be dealt with when Ohmic heating ceases to be significant. Assuming that the loop voltage is about constant, as has been observed experimentally until now, the best criterion to be followed in order to have a strong Ohmic heating rate is to have a major radius with the lowest possible values. An essential requirement to achieve ignition condition is the degree of plasma purity that has to be high as discussed in *Coppi, et al.* (2013). This restricts the spectrum of plasma regimes with which IGNITOR has to operate in order to fulfill its main objectives. Therefore while following the progress made in analyzing various transport regimes the main attention remains devoted to the high density L-regime discovered originally by Alcator that can be reliably obtained and to the I-regime that continues to be the subject of a series of investigations whose results are promising. In both regimes the observed degrees of purity are well within the limits required for ignition.

6.2.1 IGNITOR components issues, assembly and welding procedures

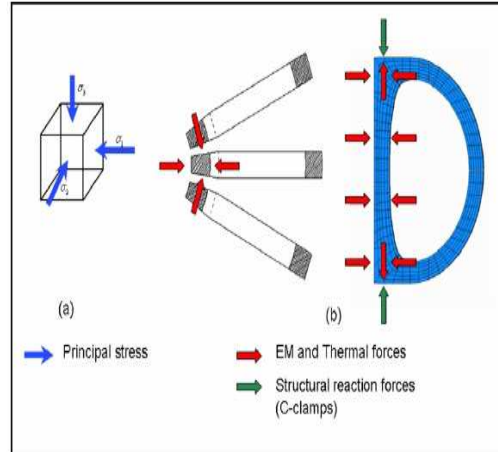


Figure 6.6: “Bucking and Wedging” solution. The objective is to minimize the unbalance between the principal stress components.

A key structural solution that has made the present design of the IGNITOR machine possible, that combines a remarkably low major radius and the ability to produce plasma currents up to 10-11 MA with realistic degrees of stability, is the mechanical collaboration between the central solenoid and the toroidal magnet. This is the so-called “bucking and wedging” of the toroidal magnet coils for their inner vertical legs that are subjected to a radial electromagnetic force toward the (vertical) axis of symmetry. Considering a cross-section on the equatorial plane, with the bucking (against the central solenoid) and wedging solution the coils are subjected to compressional forces both in the radial and tangential directions shown in Fig. 6.2.1.

The toroidal magnet system is subdivided into 12 sectors in Fig. 6.2.1. Each sector contains 20 coils. The outer supporting structure consists of the so-called C-clamps surrounding the toroidal coils with exception of their vertical leg. The total current in the toroidal magnet is 87.12 MA \rightarrow turn and corresponds to a current of 363 kA in each turn.

The plasma chamber in Fig. 6.7 is a demanding system to design as it has multiple functions, has to operate under different and extreme conditions and most important has to withstand the forces associated with macroscopic disruptions of the plasma column. Figure 6.7 shows from the top view the compact design of IGNITOR with the twelve sectors at six unions.

In fact, the evaluation of both these forces and of the number of the disruptions that can take place during the expected lifetime of the machine is subject to relatively large uncertainties. The thick plasma chamber as designed (with a varying mantle thickness from 2.6 to 5.2 cm) can

withstand a limited number of large disruptions that, taking into account the success achieved (in particular by the DIII-D machine) in preventing the development of disruptions at their onset by appropriate feedback systems, can be considered as realistic. The plasma chamber is mechanically supported by the C-clamps and provides the mechanical support for the Molybdenum tiles (actually, a variety of relevant materials is being constantly examined for these) that are in contact with the plasma. As indicated later, the replacement of the tiles during the operating phase of the machine is carried out by a dedicated robotic system.

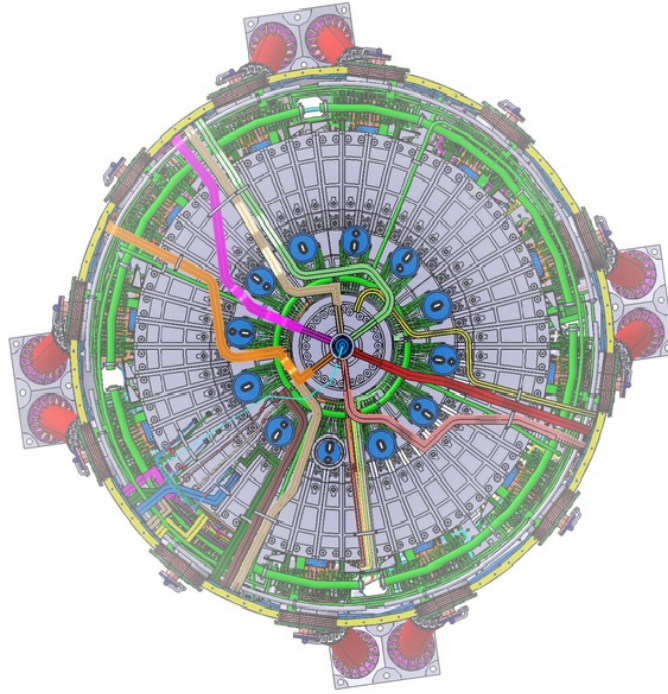


Figure 6.7: View from above the core of the IGNITOR machine. The subdivision of it into 12 modules is evident.

Given the importance of avoiding stress concentrations and considering other adopted machine design criteria, a great deal of attention has been devoted to preparing a detailed procedure for the various phases of assembly of the machine and for the welding of the plasma chamber. Two important phases are: i) the joining of 30° adjacent sectors, whose main components are a sector of the plasma chamber and the corresponding toroidal field coils and C-clamps package, until a 180° “super sector” is completed. This phase is to be carried out in a specifically equipped site away from the site in which the machine has to be operated; ii) the joining the two 180° super sectors that involves carrying out the final two weldings of the plasma chamber remotely by an appropriate robotic system. Following this joining, the high precision mechanical coupling process of the toroidal magnet with the central solenoid can be undertaken.

The equipment for the assembly of the machine in its different phases has been designed adopting solutions that permit the handling of the heavy machine components with relative ease

shown in Fig. 6.8a,b. TIG welding with and without filler material is envisioned to join adjacent sectors of the plasma chamber and to be carried out from the outside.

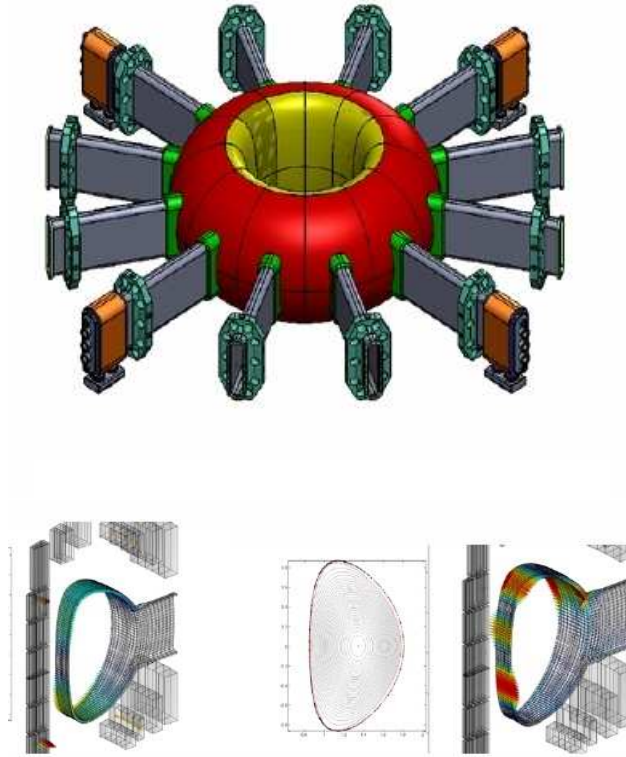


Figure 6.8: (a) Plasma chamber with access ports in IGNITOR. (b) Plasma configurations and current densities in 3D structures for the simulation of the control action after imposing an initial centroid vertical displacement of 3 cm at 2.2 ms (top) and at 32.2 ms (bottom).

6.2.2 Robotics criteria

Robotics is a fundamental element in the construction and operation of the machine: it plays a key role in two phases of the machine life: during its construction, for the closing of the plasma chamber, and during the phase in which experiments are carried out for maintenance operations. Given the different functions and constraints in either case robotics system with different characteristics of operation will be adopted.

During the final machine assembly the closing of the plasma chamber can be performed only using a robot capable of operating through a narrow vertical opening (a diagnostics port) and of

performing the delicate welding of the two 180° sectors of the machine. The robot will have to be sufficiently rigid to support the welding equipment and will have to be coupled to sensors and instruments in order to follow the welding path with great accuracy. This is an absolute necessity in order to guarantee the correct positioning of the welding structure and the execution of a weld of the highest quality.

During the operation of IGNITOR a robot with many degrees of freedom will ensure all forms of ordinary and out of the ordinary maintenance, allowing the substitution of damaged antennae and tiles. The robot will have to be able to operate within the plasma chamber through a relatively narrow access port and its path needs to extend through the entire plasma chamber. The robot will carry a “wrist” with 3 degrees of freedom and one or more dedicated grippers that would allow it to perform a sensed and adaptive grip. This is needed in order to secure and unsecure critical elements of the machine structure.

6.2.3 Nonlinear feedback control simulations with 3D structures and disruption studies

The nonlinear plasma evolution in presence of conductors is a complex event, which requires in principle extremely detailed models to be developed. Presently, several modeling approaches are available for the analysis of the electromagnetic interaction between the plasma and the conductors [Albanese and Villone (1998), Portone, et al. (2008), Czarney and Huijsmans (2008), Villone, et al. (2010)]. However, none of them can be applied to all cases of interest, due to specific limitations and ranges of applicability. In particular, codes solving linearized plasma equations are conveniently used in the feedback controller design. However, they cannot analyze a nonlinear plasma evolution characterized by large displacements and/or a wide excursion of the relevant plasma parameters. To this purpose, a new computational tool has been developed (CarMaONL [Czarney and Huijsmans (2008)]), that can describe the nonlinear evolution of axisymmetric plasmas through equilibrium points, in the presence of three-dimensional conducting structures. This allows an electromagnetic self-consistent treatment of plasma evolution during the events for which the usual linearized approximation may be no longer valid. The formulation is in the stream of the CarMa code [Czarney and Huijsmans (2008)], using a coupling surface to describe the electromagnetic interaction between the plasma and the conductors. The mathematical model and the numerical formulation is presented in Villone, et al. (2013). In particular, the 3D passive structures are efficiently modeled by the integral formulation of Villone, et al. (2013). The results of the analysis made for IGNITOR by means of a dedicated upgrade of CarMaONL are presented, including the position–shape current–integrated feedback controller inside the code [Albanese and Rubinacci (1988)].

As a reference 11 MA scenario we describe the equilibrium configuration is characterized by a plasma current $I_p = 11$ MA, poloidal beta $\beta_p = 0.203$, internal inductance $l_i = 0.818$, radial position of the current centroid $R_C = 1.299$ m. The plasma region is discretized with a 2D triangular mesh made of 5704 nodes, which coincides with the number of nonlinear equations

solved at each time step; the trace of the coupling surface $\partial\Omega$ is a line made of a set of 309 edges of such triangles, just inside the vacuum chamber.

The plasma configurations and current densities in 3D structures at two times are described in *Coppi, et al. (2013)*. The *Coppi, et al. (2013)* simulations predict the plasma disruption features and the evaluation of the EM loads associated with these events are well controlled in the machine operation scenarios and the design of in-vessel components as the EM loads produced by these events are by far the largest among those that in-vessel components must withstand. On the basis of experimental data from existing machines, the range of expected variation of the main parameters characterizing disruptions is estimated. That is, the thermal and current quench time, the evolution of plasma current (\hat{A} and l_i), the safety factor limits, the halo current fraction and the radiated heat fraction. The MAXFEA axisymmetric 2D MHD code has been used to evaluate the effects, on the induced currents and the EM loads, of variations of the disruption parameters.

6.2.4 Anomalous transport processes including self-organization for fusion burning regimes in IGNITOR

The most advanced scenario of operation for the IGNITOR experiment refers to a toroidal field on axis $B_T \approx 13$ T and $I_p \approx 11$ MA [see *Coppi, et al. (2013)*]. A special version of the JETTO equilibrium transport code [*Airolidi and Cenacchi (1997)*] was developed for the analysis of the plasma regimes to be produced by IGNITOR and employed by considering thermal transport coefficients that include (“profile consistency” [*Coppi (1980)*] criteria and constraints. Then the results (in particular, density and temperature profiles) obtained by applying different models of the electron thermal diffusion have been compared with each other. In these models the ion thermal diffusion is assumed to be represented by a collisional (neoclassical) coefficient, increased by a fraction of the electron diffusion. The first considered model assumes the *Coppi and Mazzucato (1979)* diffusion coefficient to which an appropriate fraction of a coefficient associated with the excitation of the ubiquitous modes [*Coppi, et al. (1992)*] is added.

By operating at optimized plasma parameters ($\langle n_e \rangle \approx 4.7 \times 10^{20} \text{ m}^{-3}$, $\langle Z_{\text{eff}} \rangle \approx 1.2$) ignition is achieved shortly after the end of the current ramp (at $t = 4.75$ s, where the end of current ramp occurs at $t = 4$ s). Similar optimized plasma parameters, by using a mixed Bohm-gyroBohm model, lead to obtain a delay of ignition by ≈ 1.2 s. The poloidal beta is $\beta_p \approx 0.2$ in both cases.

More recently the so-called “Coppi-Tang” model, used to predict plasma profiles and parameters for the ITER experiment [*Casper, et al. (2010)*] was applied. In this case ignition is achieved at $t = 4.5$ s and the “safety factor” $q(\psi)$ remains well over unity in the central part of the plasma column. In the following Fig. 6.9 the obtained energy confinement times are compared to the ITER97L scaling.

Tri-dimensional structures of the thermonuclear instability and control by ICRH

A surprising result of the most recent theory [*Coppi (2014)*] of the thermonuclear instability that can take place in D-T plasmas close to ignition is that this develops with tri-dimensional

structures emerging from an axisymmetric toroidal confinement configurations. These are helical filaments that are localized radially around a given rational magnetic surface [Coppi (2014)]. Until now well known analyses of the fusion burning process of magnetically confined plasmas have been carried out by $1 + \frac{1}{2}$ D transport codes. Therefore new analyses, drastically different from the one performed as a first approach to the problem and described in the following, will have to be developed.

The ICRH system is to be used as an independent means to control the plasma temperature, to accelerate the achievement of ignition in the extended first wall configuration with $B_T = 13$ T with $I_p = 10 - 11$ MA, and to facilitate the transition to the I-regime in the double X-point plasma configuration ($B_T = 9 - 13$ T with $I_p = 6 - 10$ MA). The thermonuclear instability develops at ignition with high-peak densities ($n_0 \cong 10^{21} \text{m}^{-3}$), and relatively low temperatures when the complete self-heating of the plasma by the fusion-produced α -particles takes over. This can lead to an increase of its plasma pressure. Then, internal plasma modes may be excited and saturate the thermonuclear instability at acceptable levels without external intervention.

In the case where an internal process may not be effective, a scenario is considered whereby IGNITOR is led to operate in a slightly subcritical regime, i.e. the plasma parameters are so chosen that the thermonuclear heating power is slightly less than the power lost, and a small fraction of ^3He is added to the optimal Deuterium-Tritium mixture. The difference between power lost and heating is compensated by additional ICR heating that should be able to energize the minority species (minority ion heating scheme) directly, which transfers the power to the main plasma species by collisions.

H-regime with reduced machine parameters: zero-dimensional model analysis

While making extensive use of the JETTO code, we have developed an improved zero-dimensional code solving the relevant thermal energy balance equations, and used it at first for the analysis of operation scenarios in the H-regime at reduced parameters ($B_T = 8$ T, $I_p = 5$ MA) referring to a double-null configuration (geometry of the last closed magnetic surface with two X-points) and plasma profiles with pedestals at the edge. Access to the H-regime requires an input power $P_{in} = P_{ohm} + P_{ICRF} + P_\alpha$ higher than a threshold value P_{thr} for which the expression given by the latest multi-machine ITPA scaling law, $P_{thr,08}$ [Martin, *et al.* (2008)], is employed. This condition sets a lower limit in terms of input power on the operating window available. An upper limit is set by the maximum power that the ICRF system can deliver, which is about $P_{ICRF} \approx 10$ MW at the reduced resonant frequency for operation at $B_T = 8$ T. We then find that a somehow limited operating window exists for values of the fusion gain parameter up to $Q \approx 1$; typical values for the central electron density and temperature are $n_{e0} \approx 3.4 \times 10^{20} \text{m}^{-3}$ and $T_{e0} \approx 10.7$ KeV respectively. A wider window of operation is obtained if the threshold power for accessing the H-regime is lower than that predicted by $P_{thr,08}$ [Martin, *et al.* (2008)]. Recent experiments on JET [Maggi, *et al.* (2014)] with a new metallic beryllium/tungsten wall have shown a significant reduction of P_{thr} and how this effect is correlated with low values of Z_{eff} . A reduction of P_{eff} may then be expected also for IGNITOR, that is designed to operate at low values of Z_{eff} .

ICRH and dedicated diagnostics systems

ICRH system injecting power in the frequency range 80 to 115 MHz is designed to accelerate the plasma ignition and facilitate the access to high confinement regimes such as the H and I regimes. The reference plant configuration of the system is shown in Fig. 6.9 and the following operation scenarios have been considered: a) 115 MHz: 13 T, 11 MA full performance scenario; b) 80 MHz, 9 T, 6-7 MA reduced performance scenario.

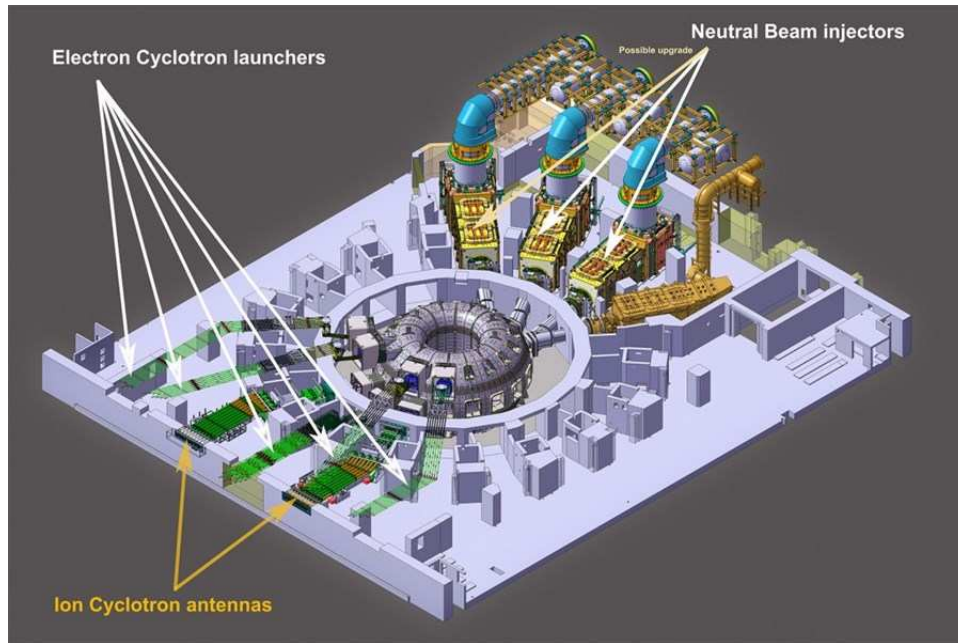


Figure 6.9: Electrical configuration of the system: the indicator scheme is relevant to 1 module and sketches the main components of the plant and their connections.

In order to have high flexibility of operation and to optimize the launch of the RF power into the plasma, the RF system has been conceived with a modular configuration, with each module based on 4 RF generators capable to operate in the frequency range indicated above.

Note that: i) the 80 MHz; is the central frequency of the selected generators and around this value the max power obtained by each unit is 2 MW; ii) the 115 MHz; this frequency is located at the upper side of the generators bandwidth and, consequently, the generated power drops down to 1 MW per unit.

The Ion Cyclotron Resonance Heating (ICRH) System is based on 2 modules with the following main characteristics: N° of Generators 8; N° of Antennas 4; Frequency Range (MHz): $80 \div 115$; Generated RF Power (MW): $16 \div 8$; RF Power at the Plasma $12.8 \div 6.4$; Pulse Length (sec) : 4; Duty Factor: $1/200$; Type of Generators: Cavity Coupled RF Tetrode; Type of Antenna: 4 Current Strap.

One of the most critical issue of the system is the safe transfer of the power to the plasma in presence of vacuum and high VSWR. For this reason the max electrical field in the vacuum region of

the transmission line and straps has been limited at 5 kV/cm with the consequent limitation of the power per strap at 400 kW. This value nicely fits the RF generated power in the full performance regime (13 T, 11 MA, 115 MHz, 8 MW at the generators). In the reduced performance regime (9 T, 6-7 MA, 80 MHz, 16 MW at the generators) the availability of the generated power will allow an increase the power per strap up to 800 kW through proper RF conditioning in the critical regions. A full size prototype of the Vacuum Transmission Line (VTL), placed between the port flange and antenna straps, has been manufactured and electrically tested; high voltage tests, at different vacuum and voltage conditions, have been carried out to check the electrical capability of the system with respect to the high voltage (12 kV) and electric field (5 kV/cm), associated with the RF Power and the strong Voltage Standing Wave Ratio (VSWR) of the plasma. A precise guiding system of the rigid coaxial cables and an innovative quick latching system have been verified and a perfect fitting with the Beryllium copper (BeCu) spring electrical contacts has been obtained.

Dedicated diagnostics systems

The Second Harmonic Interferometer (SHI) [Brandi and Giammanco (2007)] is developed and used for the interferometric measurements of the plasma density which is not sensitive to vibrations and mechanical noise. The SHI is composed of two optical units externally connected through optical fibers and the laser, the detectors and all the electronics can be placed in a separated, shielded room. The positioning of the different harmonic chords is essential so as to ensure that the whole machine is monitored. The SHI includes a section for the measurement of the Faraday rotation along the same path of the integrated electron density measurement.

The plasma ion temperature is evaluated through high-resolution spectroscopy, by measuring the Doppler broadening of the impurities atomic lines (usually O-IV or O-V). The low concentration of impurities expected in the machine does not present an insurmountable problem for the current diagnostics technology.

6.3 Superconducting Components of the IGNITOR Machine

Intermediate temperature superconducting cables have been adopted for the largest poloidal field coils of IGNITOR. The MgB₂ strands by Columbus Superconductors [Coppi, *et al.* (2013)] can achieve the target specifications for the considered vertical coils, with about 5 meters of outer diameter and maximum field on the conductor < 5 T. The cable design includes about 300 MgB₂ multifilamentary strands of 1 mm in diameter and a copper tube for the He-gas flow in the center. Significant improvements in the design and electrical properties allow higher critical current densities and better current sharing properties between the different strands than previously reported.

6.4 Dynamics of Geomagnetic Storms and Substorms with the WINDMI Model

Potential and critical issues are the basis of a comprehensive D-³He fueled FRC reactor design called “ARTEMIS” (after Apollo’s sister in Greek), which offers an attractive prospect of fusion power development for the 21st century. The ARTEMIS fusion reactor is inherently safe and environmentally acceptable in view of the low radioactivity and fuel resources. Furthermore, the estimated cost of electricity is relatively low compared to a light water reactor. An experimental research program needed to develop the D-³He fueled FRC fusion reactors is discussed by *Momota and Tomita* (1992). Magnetic reconnection is a common mechanism or phenomena in space plasmas, such as coronal mass ejections and magnetospheric substorms and also a mechanism of confinement degradation due to violation of magnetic surfaces in magnetically-confined plasmas [*Biskamp* (2000), *Drake* (2001), *Yamada, et al.* (2010)].

6.5 Impure Modes in Auroral Plasma Called Auroral Beads

Auroral beads indicate that shear-flow interchange instability in nightside magnetotail triggers substorm onset *Derr, et al.* (2019). A geometric wedge model of the near-earth nightside plasma sheet is used to derive a wave equation for long-wavelength buoyancy waves which transmit $\mathbf{E} \times \mathbf{B}$ sheared zonal flows along magnetic flux tubes. Discrepancies with the wave equation result in *Kalmoni, et al.* (2015) for shear-flow ballooning instability are discussed. The shear-flow interchange instability is responsible for substorm onset. The wedge wave equation is used to compute dispersion relations and growth rates in the midnight region of the nightside magnetotail around 9-12RE where the instability develops for comparison with the growth rates of auroral beads characteristic of geomagnetic substorm onset. Stability analysis is performed for the shear-flow interchange modes, and a brief discussion of nonlinearity follows.

6.5.1 Analysis of the bimodal nature of solar wind — magnetosphere coupling

Early analysis of auroral substorm and storm data was based on the linear prediction filter relating the solar wind electric field and the geomagnetic activity defined by the AL index. The data was both bimodal and dependent on the level of the magnetosphere activity. Early studies truncated the prediction filter to a five-parameter model containing two low-pass-filtered delta functions of arbitrary amplitude and delay time. Subsequent analysis by *Smith and Horton* (1998) on the nature of the bimodal response developed the five-parameter model to quantify the effects of the level of geomagnetic activity on each of the modes of the filter. All levels of activity, the

second mode, occurring at ~ 1 hour, is relatively unchanged. The first mode, however, has a one-parameter dependence on the level of activity in the magnetosphere. The amplitude of the first mode was shown to increase with respect to activity, and this dependence is sufficient to characterize the changing properties of the magnetosphere with respect to the level of the solar wind activity.

6.5.2 Real-time predictions of geomagnetic storms and substorms: Use of the Solar Wind Magnetosphere–Ionosphere System model

A low-dimensional plasma physics nonlinear dynamical model of the coupled magnetosphere–ionosphere system, called the Real-Time Solar Wind Magnetosphere–Ionosphere System (WINDMI), is able to predict AL and Dst values approximately one hour before geomagnetic substorm and storm events. Subsequently, the 10-min ground-based measurements compiled by World Data Center, Kyoto, are compared with model predictions (<http://orion.ph.utexas.edu/~windmi/realtime/>). WINDMI model runs are also available at the Community Coordinated Modeling Center (<http://ccmc.gsfc.nasa.gov>). The performance of the Real-Time WINDMI model is quantitatively evaluated for 22 storm/substorm event predictions from February 2006 to August 2008. Three possible input solar wind–magnetosphere coupling functions are used in WINDMI: (i) the standard rectified coupling function, (ii) a function due to Siscoe, and (iii) a function due to Newell. Model AL and Dst predictions are validated using the Average Relative Variance (ARV), Correlation Coefficient (COR), and Root Mean Squared Error (RMSE). The Newell input function yields the best model AL predictions by all three measures (mean ARV, COR, and RMSE), followed by the rectified, then Siscoe input functions. Model AL predictions correlate at least 1 standard deviation better with the AL index data than a direct correlation between the input coupling functions and the AL index. The mean Dst ARV results show better prediction performance for the rectified input than the Siscoe and Newell inputs. The mean Dst COR and RMSE measures do not clearly distinguish between the three input coupling functions.

6.6 Private Sector Company TAE in Irvine, California, Linear Fusion Machine

Private sector company in Irvine, California, linear fusion machine *Norman* and produces record mirror-confined deuterium plasmas through planetary magnetospheres-like processes.

When the interplanetary magnetic field originating at the sun contains a southward magnetic field component, the solar wind can cause magnetic reconnection on the dayside of the earth, followed by nightside reconnection in the magnetotail “Interplanetary magnetic field and the auroral zones”, n.d). This deposits energy in the magnetotail and disrupts the equatorial current sheet, initiating a sequence events which leads to the formation of aurorae in the E-layer of the

ionosphere by accelerating plasma towards the polar regions of the earth [Coppi, *et al.* (1966), Kivelson and Russell (1995), Wolf (1995), Angelopoulos, *et al.* (2008a,b), De Zeeuw, *et al.* (2004), Zou, *et al.* (2010), McPherron, *et al.* (2011), Sergeev, *et al.* (2011), Forsyth, *et al.* (2014)]. Such a sequence of events is referred to as a magnetic substorm. At the onset of magnetic substorms, the most equator-ward auroral arc suddenly brightens, followed by breakup of the arc and pole-ward expansion [Akasofu (1964) Donovan, *et al.* (2008)]. In the minutes leading to the breakup, small periodic fluctuations in the aurora aligned with magnetic longitude form [Nishimura, *et al.* (2014)]. These fluctuations have come to be called (auroral beads Henceforth, “longitudinal” will be used to refer to magnetic longitude. Auroral beads have been found to be likely pervasive in onset arcs, and the exponential growth of the beads indicates that a plasma instability in the magnetosphere is responsible for substorm onset [Gallardo-Lacourt, *et al.* (2014), Kalmoni, *et al.* (2017)].

All-Sky Imagers (ASIs), which are a part of the NASA THEMIS mission to uncover the sequence of events which occur in the first few minutes of substorm onset, are distributed across North America, as seen in Fig. . They have a 1 km spatial resolution, and 3 s cadence image capturing capacity, and respond to 557.7 nm emissions. This spatio-temporal resolution is succinct to capture the pertinent data for analyzing auroral bead structures for the green emissions corresponding to aurora at an altitude of approximately 110 km, namely the E-layer [Mende, *et al.* (2008), Burch and Angelopoulos (2008)].

Motoba, *et al.* (2012) used ASI data from auroral beads in the northern and southern hemispheres, and proposed a common magnetospheric driver. Ultra-low frequency waves occurring within minutes of substorm onset are observed in the magnetosphere at frequencies similar to those of the auroral beads, and a single event was analyzed by Rae, *et al.* (2010) to demonstrate that the beading is characteristic of a near-earth magnetospheric instability triggering a current disruption in the central plasma sheet. Of the examined instabilities, cross-field current instability and shear-flow ballooning instability were the only two consistent with the analytical results. Kalmoni, *et al.* (2015) used the ASI data for substorm events over a 12-hour time span throughout the auroral oval (pre-midnight sector) across Canada and Alaska to perform an optical-statistical analysis that yielded maximum growth rates for the beads as a function of longitudinal wavenumber, which were compared with theoretical calculations for growth rate dependence on wavenumber for various instabilities. Ultimately, the two mechanisms which remained unrefuted were the shear-flow ballooning instability and the cross-field current instability.

Note that wave propagation direction (eastward vs. westward) differed for the individual substorm events, but growth rates are independent of propagation direction [Nishimura, *et al.* (2016)].

Subsequently, Kalmoni, *et al.* (2015) used the T96 model [Tsyganenko (1995, 1996)] to map the wavenumbers back to the equatorial magnetosphere to obtain the corresponding magnetospheric wavenumbers $k_y \in [2.5 \times 10^{-6} \text{ m}^{-1}, 3.75 \times 10^{-6} \text{ m}^{-1}]$, or wavelength interval $\lambda_{\perp} \in [1700 \text{ km}, 2500 \text{ km}]$. The T96 model underestimates field-line stretching (and spatial scales) during the substorm growth phase, but the error is systematic, so the spatial scales can be compared between events. The arcs map to the equatorial plane mostly in the range of 9-12 RE, with field strengths less than 20 nT. The growth rates were normalized so that the spatial scales in the magnetosphere

were not an artifact of the T96 mapping. Normalization presupposes that most events were caused by the same instability. If each event was caused by a different instability, normalization would be unjustified.

Of the two instabilities which were not ruled out by the *Kalmoni, et al.* (2015) analysis, the shear flow ballooning instability provided the best explanation of the observed beading results, corroborating previous findings along these lines [*Friedrich, et al.* (2001)]. This instability was first characterized in *Voronkov, et al.* (1997). This instability is a hybrid of the Kelvin–Helmholtz and Rayleigh–Taylor instabilities with larger growth rates operating on shorter growth time scales than pure Kelvin–Helmholtz instability. The former are driven by shear flows and the latter by earthward pressure gradients. An extensive linear analysis of such hybrid instabilities and their relation to substorms has been conducted by *Yamamoto* (2008, 2009). In particular, it was found that the hybrid waves can grow in the presence of an earthward particle energy density gradient. The auroral arc is tied to the boundary between the stretched field 91 lines and the depolarized field lines at the inner edge of the near–Earth plasma sheet. This is 92 where pressure gradients are most relevant. The spatial scale of the shear flow ballooning instability varies inversely as the size of the shear–flow region. *Kalmoni, et al.* (2015) determined that for this instability, the growth rates peak at 0.2 s^{-1} in the wavenumber regions specified above.

After setting up a simple geometric wedge model following *Wolf, et al.* (2018) for which perturbations will entail earthward flowing waves which carry the effects of the magnetospheric disturbance back to the ionosphere, we derive a wave equation for the plasma wedge which differs from that of both his original paper [*Wolf, et al.* (2018)], and that from which *Kalmoni, et al.* (2015) extracted the equation governing the shear flow ballooning instability, namely *Voronkov, et al.* (1997). *Voronkov, et al.* (1997) treated the coupling of shear flow and pressure gradient instabilities, but incorrectly perturbed the momentum equation. *Wolf, et al.* (2018), on the other hand, neglected the shear flow effect, thus obtaining low–frequency buoyancy waves which are not coupled to shear flow. Either of these alterations shifts the growth rates and, more importantly, fails to capture some of the essential qualitative features of the instability mechanism.

In summary, it appears that a shear–flow interchange instability in the midnight region of the nightside magnetopause is the more plausible link the causal chain of events which initiate substorm onset via earthward traveling buoyancy waves, and results in the aurorae in the E–layer of the ionosphere. After perturbations drive an instability, the linear equations and dispersion relations become invalid, and the full nonlinear dynamical analysis becomes necessary. This will be the nature of future work on the ballooning interchange dynamics of the flux tubes in the wedge model.

We now eliminate fast modes, assuming $\tilde{\omega}^2 \ll k_y^2 c_f^2$, retaining only those modes which play a substantial role in substorm onset. We also assume that the length scales for $\delta v_r \sim \delta$, but are small compared to r and variations in $P_0, v_0, \rho_0 \sim L$ (from which the scale for B_0 follows from equilibrium force balance). In short, we assume small shear flow width. Care must be taken to ensure that terms which involve ratios of the small parameters are not hastily dropped.

OUTLINE

- Brief Description of the Wind Driven Magnetosphere-Ionosphere (WINDMI) Model.

- Substorm trigger in the model.
- Periodic Substorms (Sawtooth Events) — Model behavior.
- Isolated Substorms — Parameter values on substorm trigger.

WINDMI Model

- An 8-dimensional state space model of the nightside Magnetosphere–Ionosphere
- Nonlinear Ordinary Differential Equation’s (ODE) result from the application of conservation laws to global energy components of the system.
- Lumped nonlinear representation of magnetosphere.
- Kinetic effects are included in a simplified manner.

The largest energy reservoirs in the magnetosphere–ionosphere system are:

- Plasma ring current energy W_{rc} .
- Geotail lobe magnetic energy W_m .
- The R1 FAC associated with the westward auroral electrojet.
- The FAC at the lower latitude closing on the partial ring current.
- Kinetic energy proportional to $\mathbf{E} \times \mathbf{B}$ perpendicular plasma flows.
- Kinetic energy K_{\parallel} due to mass flows along magnetic field lines.
- Plasma Sheet thermal energy component p_{cps} .

Table 6.2: Nominal WINDMI Parameters, estimated by modeling of the state and geometry of the nightside magnetosphere. See Table 6.3 for more parameters.

L	90 H	Inductance of the lobe cavity surrounded by the geotail current $I(t)$. The nominal value is $L = \mu_0 A_\ell / L_x^{\text{eff}}$ in Henries where A_ℓ is the lobe area and L_x^{eff} the effective length of the geotail solenoid.
M	1 H	The mutual inductance between the nightside region 1 current loop I_1 and the geotail current loop I .
C	50000 F	Capacitance of the central plasma sheet in Farads. The nominal value is $C = \rho_m L_x L_z / (B^2 L_y)$ where ρ_m is the mass density in kg/m^3 , $L_x L_z$ is the meridional area of the plasma sheet, L_y the dawn-to-dusk width of the central plasma sheet and B the magnetic field on the equatorial plane. Computations of C are given in <i>Horton</i> (1996).
Σ	8 S	Large gyroradius ρ_i plasma sheet conductance from the quasineutral layer of height $(L_z \rho_i)^{1/2}$ about the equatorial sheet. The nominal value is $\Sigma = 0.1(n_e/B_n)(\rho_i/L_z)^{1/2}$. Computation of Σ is given in <i>Horton and Tajima</i> .
Ω_{cps}	$2.6 \times 10^{24} \text{m}^3$	Volume of the central plasma sheet that supports mean pressure $p(t)$, initial estimate is $10^4 R_E^3$.
u_0	$4e - 9 \text{m}^{-1} \text{kg}^{-1/2}$	Heat flux limit parameter for parallel thermal flux on open magnetic field lines $q_{\parallel} = \text{const} \times v_{\parallel} p = u_0 (K_{\parallel})^{1/2} p$. The mean parallel flow velocity is $(K_{\parallel} / (\rho_m \Omega_{\text{cps}}))^{1/2}$.
I_c	$1.78 \times 10^7 \text{ A}$	The critical current above which unloading occurs.
α	8×10^{11}	The geotail current driven by the plasma pressure p confined in the central plasma sheet. Pressure balance between the lobe and the central plasma sheet gives $B_\ell^2 / 2\mu_0 = p$ with $2L_x B_\ell = \mu_0 I_{\text{ps}}$. This defines the coefficient α in $I_{\text{ps}} = \alpha p^{1/2}$ to be approximately $\alpha = 2.8 L_x / \mu_0^{1/2}$.

WINDMI Model input is V_{sw} and Model outputs are I_1 and W_{rc}

$$L \frac{dI}{dt} = V_{\text{sw}}(t) - V + M \frac{dI_1}{dt} \quad (6.5)$$

$$C \frac{dV}{dt} = I - I_1 - I_{\text{ps}} - \Sigma V \quad (6.6)$$

$$\frac{3}{2} \frac{dp}{dt} = \frac{\Sigma V^2}{\Omega_{\text{cps}}} - u_0 p K_{\parallel}^{1/2} \Theta(u) - \frac{pV A_{\text{eff}}}{\Omega_{\text{cps}} B_{\text{tr}} L_y} - \frac{3p}{2\tau_E} \quad (6.7)$$

$$\frac{dK_{\parallel}}{dt} = I_{\text{ps}} V - \frac{K_{\parallel}}{\tau_{\parallel}} \quad (6.8)$$

$$L_I \frac{dI_1}{dt} = V - V_I + M \frac{dI}{dt} \quad (6.9)$$

$$C_I \frac{dV_I}{dt} = I_1 - I_2 - \Sigma_I V_I \quad (6.10)$$

$$L_2 \frac{dI_2}{dt} = V_I - (R_{\text{prc}} + R_{A2}) I_2 \quad (6.11)$$

$$\frac{dW_{\text{rc}}}{dt} = R_{\text{prc}} I_2^2 + \frac{pV A_{\text{eff}}}{B_{\text{tr}} L_y} - \frac{W_{\text{rc}}}{\tau_{\text{rc}}} \quad (6.12)$$

WINDMI Physical Parameters

Model Input Solar Wind Plasma

- Measured Solar Wind parameters from ACE.
- Two functions have been found to be most useful and reliable:
- Input Coupling Function 1 (Rectified vBs (kV)):

$$V_{\text{sw}}^{\text{Bs}} = V_0 + v_{\text{sw}} B_s^{\text{IMF}} L_y^{\text{eff}}$$

- Input Coupling Function 2 (in kV) [*Newell, et al.* (2007)]:

$$\begin{aligned} V_{\text{sw}}^{\text{N}} &= V_0 + \nu_n v_{\text{sw}}^{4/3} B_T^{2/3} \sin^{8/3}(\theta_c/2) \\ V_{\text{sw}}^{\text{NP}} &= V_0 + \nu_{\text{np}} p^{1/2} v_{\text{sw}}^{4/3} B_T^{2/3} \sin^{8/3}(\theta_c/2) \end{aligned}$$

Model Outputs of the WINDMI model

- The outputs are the AL and *Dst* indices, which are compared to ground measurements.
- The AL index from the model is obtained from the region 1 current I_1

Table 6.3: WINDMI Nominal Parameters, estimated by physical considerations of the state and geometry of the nightside magnetosphere using the Tsyganenko magnetic field model. See Table 6.6 for other parameters.

τ_{\parallel}	10 min	Confinement time for the parallel flow kinetic energy K_{\parallel} in the central plasma sheet.
τ_E	30 min	Characteristic time of thermal energy loss through earthward and tailward boundary of plasma sheet.
L_1	20 H	The self-inductance of the wedge current or the nightside region 1 current loop $I_1(t)$
C_I	800 F	The capacitance of the nightside region 1 plasma current loop.
Σ_I	3 mho	The ionospheric Pedersen conductance of the westward electrojet current closing the I_1 current loop in the auroral (altitude ~ 100 km, 68°) zone ionosphere.
R_{prc}	0.1 ohm	The resistance of the partial ring current.
τ_{rc}	12 hrs	The decay time for the ring current energy.
L_2	8 H	The inductance of the region 2 current.
R_{A2}	0.3 ohm	Resistance of the region 2 footprint in the Auroral Region.
B_{tr}	5×10^{-9} T	The magnetic field in the transition region.
A_{eff}	8.14×10^{13} m ²	The average effective area presented to the geotail plasma for plasma entry into the inner magnetosphere, estimated to be $2R_E^2$.
L_y	3.2×10^7 m	The effective width of the Alfvén layer aperture, estimated to be $5R_E$.
ΔI	1.25×10^5 A	The rate of turn-on of the unloading function.

- The D_{st} signal from the model is partly given by ring current energy W_{rc} through the Dessler–Parker–Sckopke relation:

$$Dst_{W_{\text{rc}}} = -\frac{\mu_0}{2\pi} \frac{W_{\text{rc}}(t)}{B_E R_E^3}$$

- The geotail current is compared to the Magnetotail Index (MT Index) [Asikainen (2010)] via Dst

Substorm Mechanism and Control in WINDMI Model

- The trigger function controls when the substorm is initiated:

$$\Theta(u) = \frac{1}{2} \left[1 + \tanh \left(\frac{I - I_c}{\Delta I} \right) \right] \quad (6.13)$$

- The character (growth, expansion, recovery phases) is strongly controlled by the first three equations of the model:

$$L \frac{dI}{dt} = V_{\text{sw}}(t) - V + M \frac{dI_1}{dt} \quad (6.14)$$

$$C \frac{dV}{dt} = I - I_1 - I_{\text{ps}} - \Sigma V \quad (6.15)$$

$$\frac{3}{2} \frac{dp}{dt} = \frac{\Sigma V^2}{\Omega_{\text{cps}}} - u_0 p K_{\parallel}^{1/2} \Theta(u) - \frac{pV A_{\text{eff}}}{\Omega_{\text{cps}} B_{\text{tr}} L_y} - \frac{3p}{2\tau_E} \quad (6.16)$$

- Parameters in red are tuned manually in this study.

October 4 2000 Sawteeth Event I

ACE data between 3–7 October 2000

October 4 2000 Sawteeth Event II

See *Spencer et. al.* (2007, 2009) for details. Here $I_c = 10.5$ MA, $C = 105000$ F. Using oxygen O2+ with number density 20e6 per cubic meter and magnetic field 18 nT gives 107000 F.

Substorm And Pseudo–Breakup Data Set

- *Kalmoni et. al.* (2015) use a set of Substorm and Pseudo–Breakup events to study how the growth rate of auroral beads are related to possible instability mechanisms in the near–earth plasma sheet.
- We used the same set of events but studied the substorm energy and triggering conditions using solar wind and IMF as drivers.

- 17 events. Good solar wind data for 13 events. 9 events where triggering with the model is possible.
- Compared model substorm trigger time against auroral observations (Dotted vertical red lines in all figures).
- $\Omega = 10000R_E^3$ ($100 \times 20 \times 5$) for all the results.

28 November 2005 10:08 am

02 October 2008 04:29 am

15 March 2009 04:28 am

07 March 2010 05:15 am

Model Performance On Substorm Data

Table 6.4: WINDMI Model Triggering Conditions and Associated Parameters

Date	Onset (Mdl. Onset) (Δt)	Σ [S]	I_c [MA]	C [F]
28/03/2008	05:36 (05:32) (-4)	10	3.7	8000
28/11/2005	10:08 (10:08) (0)	10	4.4	10000
22/02/2006	06:26 (06:36) (+10)	10	3.7	5000
07/03/2007	05:50 (05:47) (-3)	10	3.4	5000
02/10/2008	04:29 (04:23) (-6)	10	4.9	10000
03/01/2009	04:36 (04:24) (-12)	5	3.5	7000
24/02/2009	07:32 (07:26) (-5)	5	2.5	8000
15/03/2009	04:28 (04:24) (-4)	10	3.7	5000
07/03/2010	05:15 (05:25) (+10)	10	3.7	5000

Parameter and Variable Values for Solar WIND Plasmas

- Fixing the average B_z in the central plasma sheet, the effective width L_y , and Ω , one can estimate the mass density present in the central plasma sheet from the capacitance values needed to trigger a substorm.
- The perpendicular $v_E = E \times B$ flow velocity with $B = B_z = 10$ nT goes as 100 km/s per 1 mV/m electric field.
- Need to find consistent satellite data for the average E_y or v_E .
- From the geotail current we can track how the curvature $d\hat{\mathbf{b}}/ds$ changes during the substorm development, which is a condition for ballooning instability.
- Use the critical current parameter I_c to estimate the conditions when current driven instabilities is triggered.

- The pressure gradient current I_{ps} in the model is an estimate of dp/dx , which is also related to conditions for ballooning instability.
- Need to track $\beta = 2\mu_0 nkT/B^2$.

Summary of Geotail Substorm Model

- Model is able to capture substorms. We can study onset time, possible state of magnetosphere when onset occurs.
- It is possible to infer triggering B_z conditions when ACE to Earth advance is modeled.
- We can track intermediate variables in the model and use them as a proxy to compare to satellite data.
- Previously we used only the AL index to train the model. This resulted in the parameters fluctuating somewhat unpredictably.
- Here we used the onset time as identified from auroral observations to constrain the trigger mechanism in the model, and obtained more accurate results.
- Parameter and state variable values in the model are used to establish bounds for instabilities that trigger substorm onset.

6.7 Envisioned High-Field Superconducting Experiments

An important incentive to undertake the analysis of high field superconducting experiments is the recent realization that “hybrid” high-field magnets can be fabricated using two superconducting components: MgB2 for the “low” field ($\gtrsim 10$ T) outer part and a high temperature superconductor for the high-field inner part. The advantage of an entirely superconducting machine relative to one like IGNITOR, whose high-field components involve copper magnets, is that the length of the pulse and the duty cycle are not limited by the heating of the coils. For the inner part of the toroidal magnet a helical configuration of the type proposed originally in *Coppi et al.* (1987) can be envisioned. The main function of this is to contribute to magnetic flux variation needed to induce the high toroidal currents ($I_p \gtrsim 15$ MA).

The structural analysis of the IGNITOR machine load assembly has been performed taking into account the friction coefficients at the interfaces between the significant components. The finite element ANSYS model was used to analyze the nonlinear mechanical behavior of the structure. The calculation shows stresses within the allowable limits at the operating temperature. Interlaminar shear stresses values on TFC insulation have been validated by the results of test performed by Ansaldo. Two full size IGNITOR TFC turns have been manufactured by Kabel Metal to qualify the fabrication process and the hardening of the material OFHC. Several samples of the cooling channel were machined to validate the Electron Beam (EB) welding process.

IGNITOR structural analysis show that the structural stability of the Load Assembly is assured also during the worst plasma disruptions. The production of the new turn prototypes has allowed to validate the new design concept and to optimize the process in view of the plate series production. This prototype production has been accomplished under a strict quality assurance in order to identify and record any production aspect that may affect cost and quality.

A qualitative model which includes three loops of zonal flow vs. turbulence and turbulence vs. pressure gradient is proposed for the experimentally-observed two types of limit Cycle Oscillations (LCOs) and low-intermediate-high (L-I-H) confinement transitions. The experimental evidences supporting the model and revealing the roles of turbulence and pressure-gradient-induced flows in triggering the H-mode at marginal heating power in tokamak plasmas are presented. The dominant role played by pressure-gradient-induced flows in I-phase of type-J LCO as well as I-H transition is demonstrated, along with that done by the turbulent-Reynolds stress-driven zonal flows in the L-I transition as well as I-phase of type-Y LCO. The trigger and conditions for the I-H transition are identified from the experimental observations.

High-confinement mode is essential for realization of magnetic-confinement nuclear-fusion energy application and study of nonlinear transitions among multi-equilibrium states of complex systems, such as tokamak plasmas [Wagner, *et al.* (1982)]. However, the physics mechanism for low-to-high (L-H) confinement transition is not fully understood and is still a challenge facing the fusion community.

Two kinds of LCOs have been observed on the HL-2A tokamak when the plasma approaches the H-mode. The first one is a correlation between zonal flow and turbulence. The turbulence firstly drives zonal flow, and then the enhanced zonal flow suppresses the turbulence, which is characterized by the clockwise LCO (Y-LCO) with turbulence leading the zonal flow. The second correlation is between turbulence and the shear flow dominated by pressure gradient. The shear flow first enhances and then the turbulence is suppressed, which is characterized by the counter-clockwise LCO (Y-LCO) with the shear flow prior to turbulence. The suppressed turbulence can further make edge pressure gradient steeper and then enhance the poloidal flow. This is a positive feedback, which is necessary for triggering the L-I-H transition.

An important issue has been resolved regarding the potential of ELM control for the W (tungsten) exhaust in ITER by modeling the effect on W transport of the nonlinear MHD growth during ELMs. The results have confirmed the initial conjecture that ELMs do not contribute to W exhaust, but rather the opposite, for conditions in which W neoclassical temperature screening dominates at the pedestal between the ELMs. This puts into question the viability of the controlled ELM triggering approach to provide W exhaust over a wide range of ITER H-mode plasmas, particularly those at high Q/I_p for which the separatrix density needs to be high to provide radiative divertor cooling leading to good W screening in the pedestal.

ELMy H-mode experiments at JET in 2000/mid-2002 have focused on discharges with normalized parameters for plasma density, energy confinement and beta similar to those of the ITER $Q_{DT} = 10$ reference regime ($n/n_{GW} \sim 0.85$, $H_{98(y,2)} \sim 1$, $\beta_N \sim 1.8$). ELMy H-mode plasmas have been realized reaching or even exceeding those parameters in steady-state conditions (up to ~ 5), s or $12\tau_E$) in a reproducible way and only limited by the duration of the additional heating phase. These results have been obtained (a) in highly-triangular plasmas, by increasing the average tri-

angularity δ towards the ITER reference value ($d \sim 0.5$), and (b) in plasmas at low triangularity ($d \sim 0.2$) by seeding of Ar and placing the X-point of the plasma on the top of the septum. Pellet injection from the high-field side is a third method yielding high density and high confinement, albeit not yet under steady-state conditions. In highly-triangular plasmas the influence of input power, plasma triangularity and impurity seeding with noble gases has been studied. Density profile peaking at high densities has been obtained in (a) impurity-seeded low-triangularity discharges, (b) ELMy H-modes with low levels of input power and (c) discharges fueled with pellet injection from the high field side. New ELM behavior has been observed in high-triangularity discharges at high density, opening a possible route to ELM heat-load mitigation, which can be further amplified by Ar impurity seeding. Current extrapolations of the ELM heat load to ITER show a window for Type I ELM operation. Confinement scaling studies indicate an increase in confinement with triangularity and density peaking, and a decrease in confinement with the Greenwald number. In addition, experiments in H isotope and He indicate $\tau_E \propto M^{0.19} Z^{-0.59}$. The threshold power for the LH transition in He plasmas shows the same parametric dependence as in D plasmas, but with a 50% higher absolute value.

Detailed analysis of the ELM behavior and additional thermographic measurements on the divertor targets indicate that there is a window for operation for Type I ELM discharges in ITER. Impurity seeding is an additional tool to mitigate ELMs in discharges with high and low triangularity and has no detrimental effect on energy confinement or neutron production. Pellet injection from the high-field side with a tailored injection rate has produced discharges with high density and high confinement, but more work is needed to optimize the stationarity. Discharges with strong density peaking ($n(0)/n_{\text{ped}} \sim 2$) have been obtained without pellet injection, by careful gas dosing over long time intervals. Density peaking and high- β values both favor the destabilization of NTMs due to the associated increased bootstrap current fraction. This can be a limiting factor for the confinement properties of such plasmas, unless care is taken to avoid the creation of large seed islands, induced by large first ELMs or sawteeth, or by varying the ICRH phasing. Confinement studies show an increase of energy confinement with density peaking and triangularity, but still there is a degradation of confinement with increasing Greenwald factor. Density peaking and plasma shaping have a beneficial influence on confinement. Confinement scaling studies with data from He discharges confirmed the mass dependence of the IPB98(y, 2) scaling, and combined with previous T and H studies, suggest $\tau_E \propto M^{0.19} Z^{-0.59}$. Threshold power studies in He show the same dependence on magnetic field, density and mass as for deuterium, but the absolute value is about 50% higher in He. Extensions of the results to higher currents, fields and heating powers and towards longer flat-top durations on JET are being prepared for ITER. Plasma configurations at high average triangularity have been developed, reducing the disruptive forces of the ITER-like configuration, allowing plasma operation at JET up to 4 MA/4 T, in order to study the performance at higher absolute densities and operation closer to ρ_*^{ITER} . Such plasmas require at least 25 MW of additional heating power to reach the H-mode.

Various diagnostics have been enhanced to increase the diagnostic capabilities of JET. A inboard pellet track aiming more centrally and allowing higher pellet speeds was installed to further optimize plasma fueling by high-field side pellet injection. Long-pulse scenarios were prepared with a divertor phase of over 50 s and with potential for further extensions well over 1

min, giving a new tool for studies on the stationarity of various plasma parameters and of recycling during long-time intervals.

6.8 High Magnetic Field Toroidal Fusion Machines

The IGNITOR Program maintains the objective of approaching D-T ignition conditions by incorporating systematically advances in relevant high magnetic field technology and in experiments on high density well-confined plasmas.

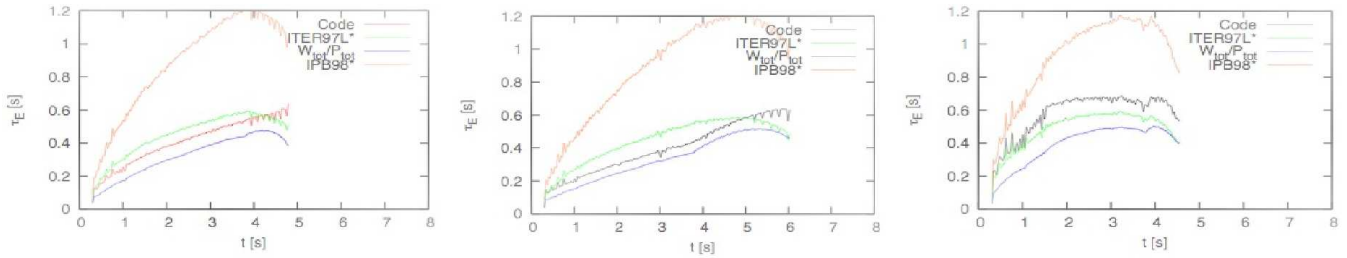


Figure 6.10: Evolution of the energy confinement time evaluated by the JETTO code $t_E = W_{\text{tot}}/P_{\text{tot}}^*$, compared to those given by the scalings ITER97L and IPB98, where $P_{\text{tot}}^* = P_W + P_a + P_{\text{aux}} - dW_{\text{tot}}/dt$. The adopted thermal energy transport models involve respectively, the so-called Coppi-Mazzucato, Bohm-gyroBohm, and Coppi-Tang transport coefficients.

Another objective is to chart the development of the high-magnetic field experiments. Considering that a detailed machine design has been carried out [Coppi, *et al.* (2013)], the advances made in different areas of the physics and technology that are relevant to the IGNITOR project are (i) Main Components Issues, Assembly and Welding Procedures; (ii) Robotics Criteria; Non-linear Feedback Control Simulations with 3D Structures and Disruption Studies; (iii) ICRH and Dedicated Diagnostics Systems; (iv) Anomalous Transport Processes Including Self-organization for Fusion Burning Regimes and Zero-Dimensional Model; (v) Tri-dimensional Structures of the Thermonuclear Instability and Control by ICRH Heating; (vi) Superconducting Components of the Machine and the Envisioned High-Field Superconducting Experiments.

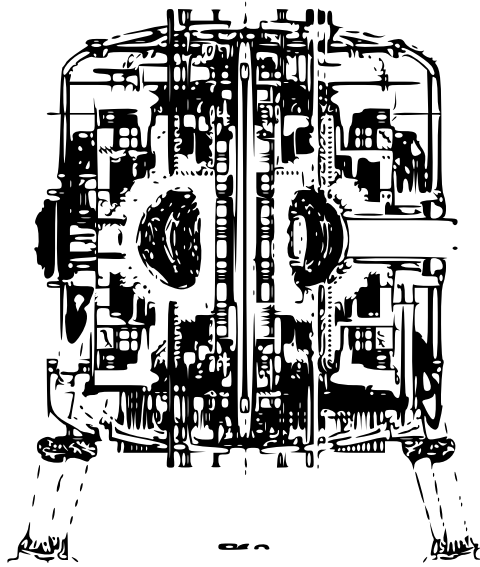


Figure 6.11: Vertical cross-section of the IGNITOR machine as presently designed.

The main objective of the IGNITOR Program is to explore the ignition conditions of magnetically confined D-T plasmas while producing significant amounts of fusion power up to about 100 MW. For this, a compact, high-field device has been designed that advances the line of high-field experiments which began with the Alcator program at MIT and was later also developed in Italy with the FT program. A relatively short but complete description and analysis of the machine core (see Figs. 6.11 and 6.12) has been given in *Coppi, et al.* (2013).

A detailed design of all the main machine components has been carried out and its results and drawings are now ready to be transferred to the industrial groups that have been identified as capable of constructing all the components of the machine core. The IGNITOR facility is expected to be operated at the Troitsk site of Rosatom and managed by the IGNIR collaboration between Italy and Russia. At this time the IGNITOR Program is the only one that has retained the objective of investigating this approach and the access to ignition conditions thanks to the regular updates of the machine design that have followed relevant advances in physics, technology and materials. The main machine parameters are included in Table 6.1 [*Coppi, et al.* (2013)].

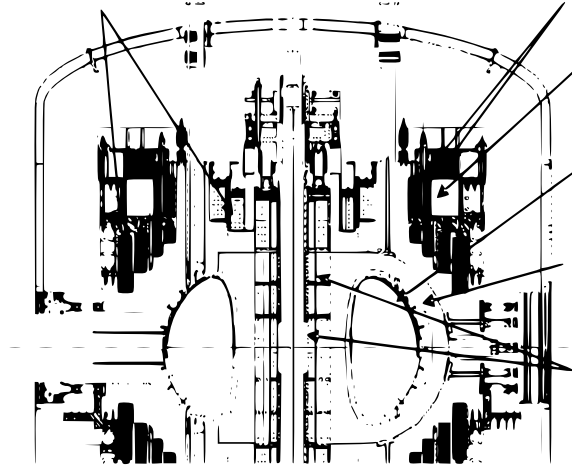


Figure 6.12: Sketch of the vertical cross-section of the IGNITOR machine where the main components are indicated.

6.9 Linear Mirror Machines and the Field-Reversed Confinement Machines

Linear Mirror Machines, as developed at the Lawrence Livermore Laboratory in California and in the Budker Institute in Novosibirsk, have unique properties that are complementary to those of the toroidal plasmas.

A plasma blob-filament (or simply a “blob”) is a localized magnetic field-aligned plasma vortex structure that is considerably denser than the surrounding background plasma and localized in the directions perpendicular to the equilibrium magnetic field B . In experiments and simulations, these intermittent filaments are often formed near the boundary between open and closed field lines, and seem to arise in theory from the saturation process for the turbulence edge instabilities. Blobs become charge-polarized under the action of an external force which causes unequal drifts on ions and electrons; the resulting polarization-induced $\mathbf{E} \times \mathbf{B}$ drifts move the vortices radially outwards across magnetic separatrix into the Scrape-Off Layer (SOL) plasma of toroidal and in mirror machines (CLM) plasmas.

High-electron temperatures T_e reduce charge exchange losses and increase fast particle-slowing down time, thereby enhancing the efficiency of plasma heating and current drive. The role of RF electron heating is critical in Fusion Power plasmas. The recent verification of RF heating is in the Field-Reversed Configuration (FRC) plasma, as described in this chapter.

High electron temperature T_e improves plasma confinement and performance. The RF electron heating study produces new insights into the physics underlying effects of unique FRC magnetic configuration

Plasma is over-dense ($\omega_{pe} > 30\omega_{ce}$). The radial profiles of the HHFW heating in the C-2

FRC plasmas are shown in Figs. 6.17–6.13 for five frequencies.

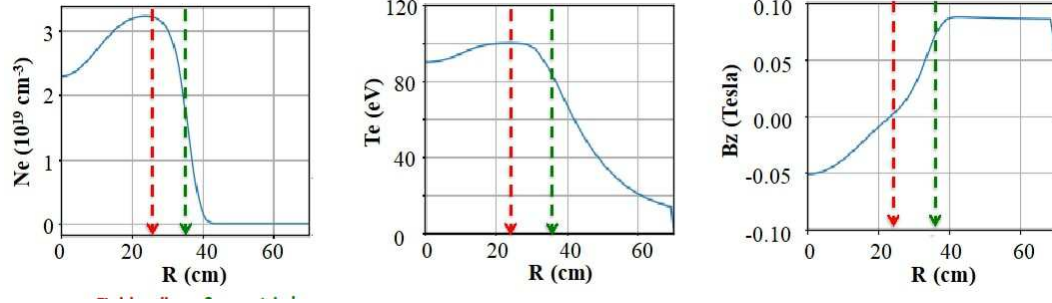


Figure 6.13: High T_e reduces charge exchange losses and increases fast particle slowing down time, thereby enhancing the efficiency of NB heating and NBCD. High T_e improves FRC plasma confinement and performance. Produces new insights into the physics underlying important effects of unique FRC magnetic configuration on traditional RF heating regimes.

For the electron heating in the Field-Reversed Configuration (FRC) in the University of California in Irvine and the TriAlpha Laboratory, the waves are:

- EBW (2.45 GHz, 5 GHz, 8 GHz, 18 GHz, and 28 GHz)
- Upper-hybrid resonant frequency (50 GHz, 55 GHz)
- Whistler wave frequency (0.5-1.0 GHz).
- Landau damping — the force acting on electrons is $F_{LD} = eE_{\parallel}$
- Transit-Time Magnetic Pumping (TTMP or MP), in which the force is $F_{MP} = -\nabla_{\parallel}(\mu B_{\parallel})$

The radial profiles of the RF waves are shown in Fig. 6.14 for the plasma parameter in Table 6.1. The machine is shown in Fig. 6.14 and is normal for the inventor Norman Rostoker.

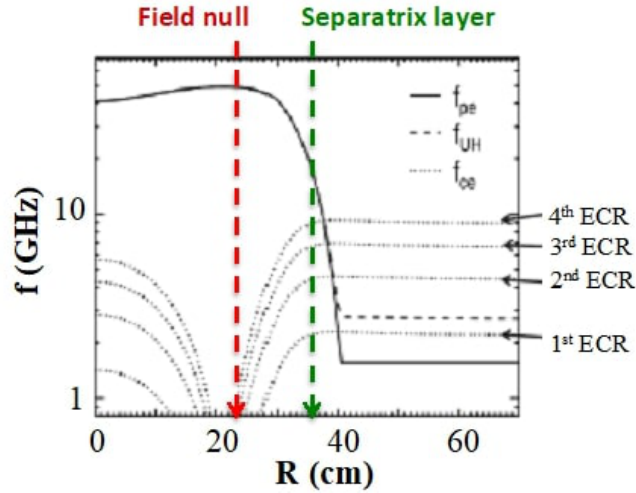


Figure 6.14: Plasma is over-dense ($\omega_{pe} > 30\omega_{ce}$) plasma. The magnetic field B drops quickly to 0 within 12 cm radial distance. In this case, the Electron Cyclotron Resonance (ECR) harmonic resonant layers are compacted into a narrow radial region and the microwaves propagate radially only for a short distance.

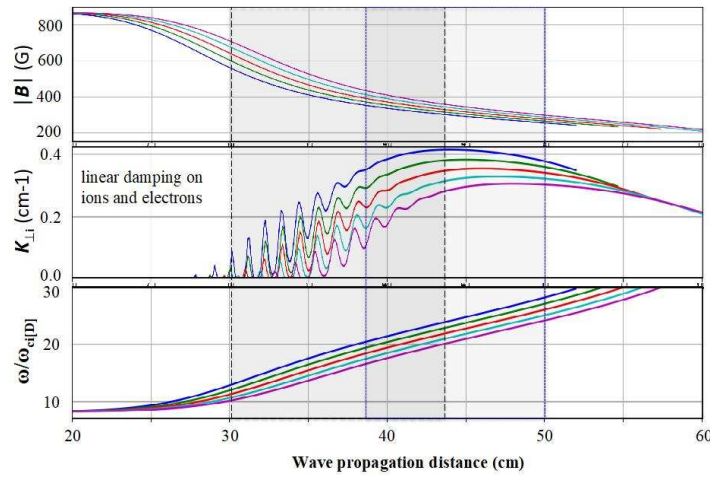


Figure 6.15: Wave propagation distance (cm) in the FRC plasma in the *Norman* machine shown in Fig. 6.14.

6.9.1 D-³He fueled FRC power plant for the 21st Century

The principle advantage of D-³He fueled fusion is the mitigation of the engineering problems produced by the 14 MeV neutrons. *Momota and Tomita* (1992) describe the requirements needed

to construct an attractive D-³He fusion reactor. The intrinsic characteristics of a field-reversed magnetic confinement is to provide a high plasma-pressure confinement machine configuration.

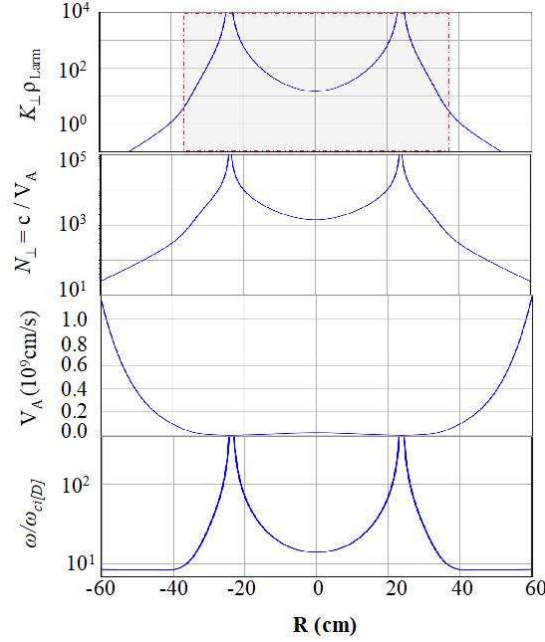


Figure 6.16: The RF wave parameters as a function of plasma radius R for the waves shown.

6.9.2 Global simulations of the Field-Reversed Configuration (FRC) fusion plasmas

Global Particle-In-Cell (PIC) code, called ANC, with electrostatic drift waves is used in simulations of the electron drift wave turbulence in C-2/C-2U plasmas [Lau, *et al.* (2017)]. The simulations show that turbulence grows up in the SOL and then spreads into the core field-reversed region in the nonlinear steady state through an inverse cascade from $k_\phi \rho_s$ from the maximum linear growth rates with toroidal mode numbers of 70 to 75 corresponding to $k_\phi \rho_s \sim 15$ to 20. The turbulence saturates with $k_\phi \rho_s \sim 5$ -10 in the SOL. In the core the spectrum peaks at $k_\phi \rho_s \sim 10$ from nonlinear coupling driven by the high level of turbulence in the scrape-off layer. In the saturated state the turbulence peak shifts from the mid-plane to the mirror regions near $z = +, -2$ m in the SOL.

New simulations with nonadiabatic electron dynamics and the Alfvén waves active are being performed. The electrostatic drift wave turbulence is consistent with the Doppler Backscatter (DBS) density fluctuation data reported by Schmitz, *et al.* (2016). The fluctuation backscatter diagnostic instrument used to measure the density fluctuations is described in Schmitz *et al.* (2014). The properties of the electrostatic drift waves in the beam driven Field-Reversed Configuration (FRC) are unstable producing a turbulent ion thermal flux. The unstable axial eigenmodes are

computed for toroidal mode number $n = 20$ axial for four machine lengths ranging from $27R_0$ to $42R_0$ where $R_0 = 26.8\text{ cm}$ is the radius of the central confinement chamber. The $k_\perp \rho_i = 2.0$ is fixed and the growth rate frequency normalized to $v_{th,i}/L$ with $L = 0.4R_0$. The growth rates range from $0.0022\Omega_{cp}$ to $0.0037\Omega_{cp}$ with even and odd mode symmetries about the center of the mirror chamber. There are flute-like modes with even parity and an odd parity modes with respect to the $z \rightarrow -z$ axial reflection symmetry about $z \rightarrow -z$. The maximum mode amplitudes occur well outside the SOL separatrix and maximum in mirror region beyond the B_{\max} at $Z/R = \pm 10$.

Typical frequency and growth rates are $\omega = -6v_{th,i}/L_s$ and $\gamma = 1.0$ to $1.2 v_{th,i}/L_s$ where $L_s = 20R_0$ the length of the field line for a typical mode with $n = 20$ corresponding to $k_s \rho_i = 0.36$ and $n = 20$ and $k_r \rho_i = 0.6$.

In the closed magnetic field region the magnetic gradient drift is opposite to the diamagnetic drift direction. Outside the magnetic curvature drift is in the same direction as the diamagnetic drift in the outer mid-plane and opposite the diamagnetic drive in the mirror throats. Contour plots of the eigenmode structures are shown in *Bao, et al. (2019)*. The maximum amplitude of the axial wave functions is in the “bad” magnetic curvature region in the formation section at $|z|/R_0 \gtrsim 15$ to 20 . The maximum of the wave function is in the two-end formation sections of the long central cell. The formation section is past the end-region mirrors cells and before the divertor end-cell region. The unstable drift waves are only strong in the SOL outside the closed FRC separatrix. The global particle-in-cell code GTC-X with the Alfvén wave coupling gives the details of the plasma waves and transport. The ITG mode is stable inside the magnetic separatrix. The linear eigenmode calculations show that the turbulent ion thermal transport is outside the field reversal region.

The impurity effects on Ion Temperature Gradient (ITG) driven instability in Transport Barriers (TBs) are numerically investigated with the gyrokinetic integral eigenmode equations in tokamak plasmas. In particular, the effects of temperature and density gradients of the main ions (ε_{T_i} and ε_{ni}) are analyzed independently to understand the physical mechanisms better, instead of keeping their ratio $\eta_i = \varepsilon_{ni}/\varepsilon_{T_i} = \text{const}$ as carried out in previous works, when the parameters of impurity ions vary. It is found that the effect of impurity ions with outwardly peaked density profiles on ITG modes depends on the competition between the destabilizing effect of the impurity density gradient L_{n_z} and the stabilizing effect induced by the dilution of main ions from impurity ions when ε_{T_i} is fixed, which is in contrast with the results for a fixed η_i . The destabilizing effects include enhancement of ITG modes and coupling to the Impurity Mode (IM) in weak ITGs (big ε_{T_i}) and strong impurity density gradient regimes. In addition, the stability boundaries for ITG modes, including high-order modes, are discussed in detail, and compared with previous works [*Fröjdh, et al. (1992)*]. Furthermore, the impurity ions with either inwardly or slightly outwardly peaked density profiles have weaker and stronger stabilizing effects on small and large poloidal wave vector $k_\theta \rho_s$ modes, respectively. However, the impurity ions with steeper outwardly peaked density profiles have stronger stabilizing effects on large $k_\theta \rho_s$ modes. Moreover, the inwardly-peaked impurity ion density profiles are beneficial for main ion confinement and impurity decumulation, due to the main (impurity) ions flowing inwardly (outwardly). Finally, analyses of eigenmode structure and the quasilinear particle flux are performed in detail. The results show that the gradients of the impurity ions have important effects — especially on higher-order ITG modes.

6.10 Mirror Confinement With Expansion Grids

Mirror confinement with expansion grids biased to reflect the escaping electrons operates as GDT at Novosibirsk and in the Tri Alpha Company machine in Irvine, California.

Over nearly 20 years, TriAlpha Energy (TAE) has raised over \$500M of private capital, allowing it to pioneer and then refine the FRC approach over a succession of experimental research devices, leading up to the present C-2W experiment, shown in Figure 1. Our long-term computational research goal is to do Whole Device Modeling, which will combine models working on many scales, with calibration and verification with experimental data from C-2W and its successors. In conjunction with experiments this will lead to a commercial fusion power plant. How quickly this will happen depends, in part on our ability to do “virtual science”.

The physics that is being studied at Tri Alpha Energy has important relevance for the publicly-funded fusion plasma science sector, because many of the concepts are complementary to those being explored in public facilities such as the NSTX-U experiment at Princeton Plasma Physics Laboratory, and the GDT experiment at Budker Institute.

6.11 Kinetic Simulation of Field-Reversed Configuration (FRC) Stability and Transport

Magnetic confinement fusion offers the prospect of a carbon-neutral, environmentally responsible and inexhaustible energy source. The present mainline approach to magnetic fusion energy is via the tokamak reactor that relies on a strong toroidal (doughnut-shaped) magnetic field to confine plasma at temperatures characteristic of the interior of stars (~ 100 million°K). The hydrogen isotopes deuterium (D) and tritium (T) fuse at these temperatures, releasing energy mainly in the form of neutrons and alpha (He^{++}). The most advanced tokamak to date, the International Thermonuclear Experimental Reactor, is designed to test and demonstrate the sustained production of fusion energy for the first time.

The magnetic field-reversed configuration (FRC) employs its magnetic field more efficiently, characterized by a much higher ratio β of the plasma kinetic pressure to the external magnetic field energy density, with averaged $\beta \sim 0.9$. This magnetic configuration is of great interest as a fusion reactor concept due to its compact, axisymmetric geometry and the potential for aneutronic fusion based on advanced fuels, such as the proton-Boron fusion reaction (p-B^{11}). A major advantage of this fuel is that there are vast quantities of Boron in the US and around the world, in contrast with Tritium, a hydrogen isotope not found naturally on Earth.

Over nearly 20 years, TriAlpha Energy (TAE) has raised over \$500M of private capital, allowing it to pioneer and then refine the FRC approach over a succession of experimental research devices, leading up to the present C-2W experiment, shown in Figure 1. Our long-term computational research goal is to do Whole Device Modeling, which will combine models working on many scales, with calibration and verification with experimental data from C-2W and its successors. In

conjunction with experiments this will lead to a commercial fusion power plant. How quickly this will happen depends, in part on our ability to do “virtual science”.

6.11.1 A New Code (ANC) and Field-Reversed Configuration (FRC) codes in context

The ANC code [Fulton (2017)] is a specialization of the Gyrokinetic Toroidal Code (GTC) [Lin, *et al.* (1998), Holod, *et al.* (2009)], and is developed in collaboration between Tri Alpha Energy and Professor Zhihong Lin, PI of the Gyrokinetic Toroidal Code (GTC) project, at UC Irvine. A New Code (ANC) and Gyrokinetic Toroidal Code (GTC) are the first codes that are being used to simulate turbulent transport in the Field-Reversed Configuration (FRC). GTC is the first fusion code to reach the teraflop speed in 2001 on the Seaborg computer at NERSC (2001), [Lin, *et al.* (2002)] and the petaflop in 2008 on the Jaguar computer at ORNL in production simulations [Xiao and Lin (2009)]. Through collaborations with computer scientists from hardware vendors including NVIDIA and Inspur/Intel, the GTC production version was the first large scale fusion code to fully utilize the heterogeneous architectures using GPU (graphic processing unit) accelerators on Tianhe-1A [Meng, *et al.* (2013)] and Titan, and using MIC (many integrated core) co-processors on Tianhe-2 [Dongarra (2013)]. GTC has been selected by the DOE Center for Accelerated Application Readiness (CAAR), a program to prepare prominent codes across all DOE supported science research portfolio for the emerging exascale computers [CAAR] such as the next generation computer Summit at ORNL. GTC has recently been ported to SummitDev, the prototype computer of Summit. GTC has received large time allocations on the supercomputers at NERSC and ORNL through the SciDAC, INCITE, ALCC, and CAAR projects.

In the DOE-funded space of turbulent plasma transport codes, the only other code which may have the capacity for global turbulence study of the FRC is the XGC-I code [Chang and Ku (2008)] at the Center for Edge Physics Simulation hosted at PPPL.

FPIC is not the first hybrid Particle-In-Cell (PIC) code to be used for global stability studies of FRCs. The HYM code [Belova, *et al.* (2001)] has been used extensively to study FRC global stability in the past, including specific applications to TAE problems. Review of existing FRC stability studies makes it clear that the global stability properties of an FRC depend intricately on the end boundary conditions [Belova (2015)], the shape of external current distributions [Yamada, *et al.* (2007)], the shape of the separatrix and the plasma profiles [Parks and Schaffer (2003)], and the level of kinetic influence [Milroy, *et al.* (2008), Barnes and Milroy (1991)]. All of these parameters may change during an FRC discharge; some of them are external actuators which may be used for feedback control. FPIC was developed by TAE because feedback and control of global stability is a requirement for the C-2W experimental program, and must work in order to achieve the TAE strategic goal. The feedback and control capability of FPIC is unique in the area of global stability PIC codes.

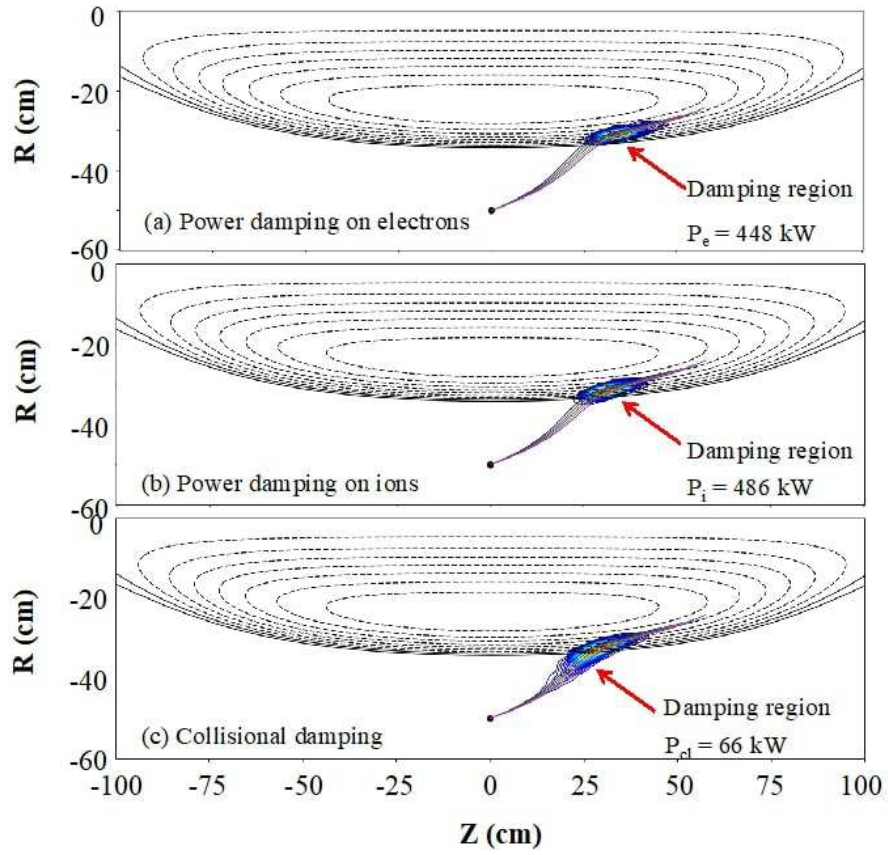


Figure 6.17: Wave propagation distance in centimeters (cm). Concentric elliptic rays from a spectrum of RF waves launched from the antennas with different initial n_{\parallel} between 4 (blue) and 6 (purple); each ray has 200 kW power at launching point. The region of significant power damping is between 30 cm and 50 cm.

TO BE ADDED

Bibliography

- [1] Airoidi, A. and Cenacchi, G. (1997). Approach to ignition in the IGNITOR experiment, *Nucl. Fusion* **37**, p. 1117, <https://doi.org/10.1088/0029-5515/37/8/I0>.
- [2] Albanese, R. and Rubinacci, G. (1988). Integral formulation for 3D eddy-current computation using edge elements, *IEEE Proc. A.* **135**, pp. 457–462, <https://doi.org/10.1049/ip-a-1.1988.0072>.
- [3] Albanese, R. and Villone, F. (1998). The linearized CREATE–L plasma response model for the control of current, position and shape in tokamaks, *Nucl. Fusion* **38**, p. 723, <https://doi.org/10.1088/0029-5515/38/5/307>.
- [4] Angioni, C. and Peeters, A. G. (2006). Direction of impurity pinch and auxiliary heating in tokamak plasmas, *Phys. Rev. Lett.* **96**, p. 095003, <https://doi.org/10.1103/PhysRevLett.96.095003>.
- [5] Angioni, C., Sertoli, M., Bilato, R., Bobkoy, V., Loarte, A., Ochoukov, R., Odstrcil, T., Pütterich, T., Stober, J. and The ASDEX Upgrade Team. (2017a). A comparison of the impact of central Electron Cyclotron Resonance Heating (ECRH) and central Ion Cyclotron Resonance Heating (ICRH) on the tungsten behaviour in ASDEX Upgrade H-mode plasmas, *Nucl. Fusion* **57**, p. 056015, <https://doi.org/10.1088/1741-4326/aa6453>.
- [6] Angioni, C., Bilato, R., Casson, F. J., Fable, E., Mantica, P., Odstrcil, T., Valisa, M., ASDEX Upgrade Team and JET Contributors. (2017b). Gyrokinetic study of turbulent convection of heavy impurities in tokamak plasmas at comparable ion and electron heat fluxes, *Nucl. Fusion* **57**, p. 022009, <https://doi.org/10.1088/0029-5515/57/2/022009>.
- [7] Asikainen, T., Maliniemi, V. and Mursula, K. (2010). Modeling the contributions of ring, tail, and magnetopause currents to the corrected *Dst* index, *J. Geophys. Res.* **115**, p. A12203, <https://doi.org/10.1029/2010JA015774>.
- [8] Bao, J., Lau, C. K., Lin, Z., Wang, H. Y., Fulton, D. P., Dettrick, S. and Tajima, T. (2019). Global simulation of ion temperature gradient instabilities in a field-reversed configuration, *Phys. Plasmas* **26**, p. 042506, <https://doi.org/10.1063/1.5087079>.
- [9] Benkadda, S., Verga, A., Tsytovich, V. N. (1995). Influence of dust on drift instability in edge tokamak plasma, *Comm. Plasma Phys. Control. Fusion* **16**, pp. 321–333, ISSN:0374–2806.

- [10] Binderbauer, M. W., Tajima, T., Steinhauer, L. C., Garate, E., Tuszewski, M., Schmitz, L., Guo, H. Y., Smirnov, A., Gota, H., Barnes, D., Deng, B. H., Thompson, M. C., Trask, E., Yang, X., Putvinski, S., Rostoker, N., Andow, R., Aefsky, S., Bolte, N., Bui, D. Q., Ceccherini, F., Clary, R., Cheung, A. H., Conroy, K. D., Dettrick, S. A., Douglass, J. D., Feng, P., Galeotti, L., Giammanco, F., Granstedt, E., Gupta, D., Gupta, S., Ivanov, A. A., Kinley, J. S., Knapp, K., Korepanov, S., Hollins, M., Magee, R., Mendoza, R., Mok, Y., Necas, A., Primavera, S., Onofri, M., Osin, D., Rath, N., Roche, T., Romero, J., Schroeder, H., Sevier, L., Sibley, A., Song, Y., Van Drie, A. D., Walters, J. K., Waggoner, W., Yushmanov, P., Zhai, K., and the TAE Team (2015). A high-performance field-reversed configuration, *Phys. Plasmas* **22**, p. 056110, <http://dx.doi.org/10.1063/1.4920950>.
- [11] Brandi, F. and Giammanco, F. (2007). Versatile second-harmonic interferometer with high temporal resolution and high sensitivity based on a continuous-wave Nd:YAG laser, *Opt. Lett.* **32**, p. 2327, <https://doi.org/10.1364/OL.32.002327>.
- [12] Breizman, B. N. and Aleynikov, P. B. (2017). Kinetics of relativistic runaway electrons, *Nucl. Fusion* **57**, p. 125002, <https://doi.org/10.1088/1741-4326/aa8c3f>.
- [13] Breizman, B. N., Aleynikov, P. B., Fontanilla, A. K., Helander, P., Oliver, H.J. C. and Sharapov, S. E. (2018). The feeder pellets and the killer pellets in a plasma, Talk presented at Joint Varenna–Lausanne International Workshop on Theory of Fusion Plasmas. Varenna. 2018–08–27–2018–08–31.
- [14] Brookman, W. M., Austin, M. E., Gentle, K. W., Petty, C. C., Ernst, D. E., Peysson, Y., Decker, J. and Barada, K. (2017). Experimental measurement of ECH deposition broadening: Beyond anomalous transport, *EPJ Web of Conferences* **147**, p. 03001, <https://doi.org/10.1051/epjconf/201714703001>.
- [15] Burhenn, R., Feng, Y., Ida, K., Maassberg, H., McCarthy, K. J., Kalinina, D., Kobayashi, M., Morita, S., Nakamura, Y., Nozato, H., Okamura, S., Sudo, S., Suzuki, C., Tamura, N., Weller, A., Yoshinuma, M. and Zurro, B. (2009). On impurity handling in high-performance stellarator/heliotron plasmas, *Nucl. Fusion* **49**, p. 065005, <https://doi.org/10.1088/0029-5515/49/6/065005>.
- [16] Casper, T. A., Meyer, W. H., Jackson, G. L., Luce, T. C., Hyatt, A. W., Humphreys, D. A. and Turco, F. (2010). Validation of the thermal transport model used for ITER startup scenario predictions with DIII–D experimental data, *Nucl. Fusion* **51**, p. 013001, <https://dx.doi.org/10.1088/0029-5515/51/1/013001>.
- [17] Casson, F. J., Angioni, C., Belli, E. A., Bilato, R., Mantica, P., Odstreil, T., Pütterich, T., Valisa, M., Garzotti, L., Giroud, C., Hobirk, J., Maggi, C. F., Mylnar, J., Reinke, M. L., *etal.* (2015). Theoretical description of heavy impurity transport and its application to the modeling of tungsten in JET and ASDEX Upgrade, *Plasma Phys. Control. Fusion* **57**, p. 014031 <http://dx.doi.org/10.1088/0741-3335/57/1/014031>.

- [18] Cerfon, A. J. and Freidberg, J. P. (2010). “One size fits all” analytic solutions to the Grad–Shafranov equation, *Phys. Plasmas* **17**, p. 032502, <https://doi.org/10.1063/1.3328818>.
- [19] Charidakos, I. K., Lingam, M., Morrison, P. J., White, R. L. and Wurm, A. (2014). Action principles for extended magnetohydrodynamic models, *Phys. Plasmas* **21**, p. 092118, <https://doi.org/10.1063/1.4896336>.
- [20] Cho, T., Pastukhov, V. P., Horton, W., Numakura, T., Hirata, M., Kohagura, J., Chudin, N. V. and Pratt, J. (2008). Active control of internal transport barrier formation due to off-axis electron–cyclotron heating in GAMMA–10 experiments, *Phys. Plasmas* **15**, p. 056120, <http://dx.doi.org/10.1063/1.2906262>.
- [21] Copenhaver, C. (1983). Axisymmetric toroidal equilibria with plasma flow, *Phys. Fluids* **26**, p. 2635, <https://doi.org/10.1063/1.864455>.
- [22] Coppi, B. and Mazzucato, E. (1979). Transport of electron thermal energy in high temperature plasmas, *Phys. Letts. A* **71**, p. 337, [http://dx.doi.org/10.1016/0375-9601\(79\)90071-9](http://dx.doi.org/10.1016/0375-9601(79)90071-9).
- [23] Coppi, B. (1980). Nonclassical transport and the ‘principle of profile consistency’, *Comm. Plasma Phys. Control. Fusion* (UK) **5**, pp. 261–269, ISSN:0374–2806.
- [24] Coppi, B., Lanzavecchia, L. and Airoidi, A. (1987). Compact ignition experiments: physics and design issues, *Comm. Plasma Phys. Control. Fusion* (UK) **11**, pp. 47–61, ISSN:0374–2806.
- [25] Coppi, B., Nassi, M. and Sugiyama, E. (1992). Physics basis for compact ignition experiments, *Physica Scripta* **45**, p. 112, <https://dx.doi.org/10.1088/0031-8949/45/2/010>.
- [26] Coppi, B., Airoidi, A., Albanese, R., Ambrosino, G., Berta, S., Bianchi, A., Bombarda, F., Cardinali, A., Cenacchi, G., Chilton, L., Clai, G., Detragiache, P., Faelli, G., Frattolillo, A., Frosi, P., Giunchi, G., Grasso, G.; Mantovani, S., Migliori, S., Penco, R., Pierattini, S., Pironti, A., Pizzicaroli, G., Ramogida, G., Rebusco, P., Rubinacci, G., Sassi, M., Villone, F., Zhou, T. C. and Zucchetti, M. (2010). *Near Term Perspectives for Fusion Research and New Contributions by the IGNITOR Program*, pp. 1–12. Proc. 23rd IAEA Fusion Energy Conf. (Daejeon, Republic of Korea) Conf. ID: 38091 (2010) (Vienna: IAEA) Overview Paper OV/P–2.
- [27] Coppi, B., Airoidi, A., Albanese, R., Ambrosino, G., Bombarda, F., Bianchi, A., Cardinali, A., Cenacchi, G., Costa, E., Detragiache, P., De Tommasi, G., DeVellis, A., Faelli, G., Ferrari, A., Frattolillo, A., Frosi, P., Giammanco, F., Grasso, G., Lazzaretti, M., Mantovani, S., Migliori, S., Pierattini, S., Pironti, A., Ramogida, G., Rubinacci, G., Sassi, M., Tayani, M., Tumino, A. and Villone, F. (2013). New developments, plasma physics regimes and issues for the IGNITOR experiment, *Nucl. Fusion* **53**, p. 104013, <https://doi.org/10.1088/0029-5515/53/10/104013>.

- [28] Coppi, B. (2014). Presentation at the Sherwood Theory Meeting, San Diego, CA, April 2014.
- [29] Coppi, B. (2015). MIT (LNS) Report HEP 15/07 To be submitted to AIP Proceedings Book Norman Rostoker Memorial Symposium Proceedings University of California, Irvine 2015.
- [30] Czarny, O. and Huijsmans, G. (2008). Bézier surfaces and finite elements for MHD simulations, *J. Comput. Phys.* **2277**, pp. 7423–7445, <https://doi.org/10.1016/j.jcp.2008.04.001>.
- [31] D’Ippolito, D. A., Myra, J. R. and Zweben, S. J. (2011). Convective transport by intermittent blob–filaments: Comparison of theory and experiment, *Phys. Plasmas* **18**, p. 060501, <https://doi.org/10.1063/1.3594609>.
- [32] Decker, J., Peysson, Y., Hillairet, J., Artaud, J.–F., Basiuk, V., Becoulet, A., Ekedahl, A., Goniche, M., Hoang, G. T., Imbeaux, F., Ram, A. K. and Schneider, M. (2011). Calculations of lower–hybrid current drive in ITER, *Nucl. Fusion* **51**, p. 073025, <http://dx.doi.org/10.1088/0029-5515/51/7/073025>.
- [33] Don, et al. (1999).
- [34] Dong, J–Q., Horton, W. and Dorland, W. (1994). Isotope scaling and η_i mode with impurities in tokamak plasmas), *Phys. Plasmas* **1**, p. 3635, <https://doi.org/10.1063/1.870942>.
- [35] Doyle, E. J., Houlberg, W. A., Kamada, Y., Mukhovatov, V., Osborne, Polevoi, A., Bateman, G., Connor, J. W. Cordey, J. G., Fujita, T., Garbet, X., Hahm, T. S., Horton, L. D., Hubbard, A. E., Imbeaux, F., Jenko, F., Kinsey, J. E., Kishimoto, Y., Li, J., Luce, T. C., Martin, Y., Ossipenko, M., Parail, V., Peeters, A., Rhodes, T. L., Rice, J. E., Roach, C. M., Rozhansky, V., Ryter, F., Saibene, G., Sartori, R., Sips, A. C. C., Snipes, J. A., Sugihara, M., Synakowski, E. J., Takenaga, H., Takizuka, T., Thomsen, K., Wade, M. R., Wilson, H. R., ITPA Transport Physics Topical Group, ITPA Confinement Database and Modeling Topical Group, and ITPA Pedestal and Edge Topical Group. (2007). Chapter 2: Plasma confinement and transport, *Nucl. Fusion* **47**, p. 099801, <http://dx.doi.org/10.1088/0029-5515/47/6/S02>.
- [36] Fontana, M., Porte, L. and Cabrera, P. Molina (2017). Correlation electron cyclotron emission diagnostic in TCV, *Rev. Sci. Instrum.* **88**, p. 083506, <https://doi.org/10.1063/1.4997075>.
- [37] Fontana, M., Porte, L., Coda, S., Sauter, O. and The TCV Team (2018). The effect of triangularity on fluctuations in a tokamak plasma, *Nucl. Fusion* **58**, p. 024002, <https://doi.org/10.1088/1741-4326/aa98f4>.
- [38] Fontanilla, A. K. and Aleynikov, P. B. (2017). Lifetime and universal distribution of seed runaway electrons, *Phys. Plasmas* **24**, p. 112509, <https://doi.org/10.1063/1.5001931>.

- [39] Frójdth, M., Liljestrom, M. and Nordman, H. (1992). Impurity effects on η_i mode stability and transport, *Nucl. Fusion* **32**, p. 419, <https://doi.org/10.1088/0029-5515/32/3/I06>.
- [40] Fülöp, T. and Nordman, H. (2009). Turbulent and neoclassical impurity transport in tokamak plasmas, *Phys. Plasmas* **16**, p. 032306, <https://doi.org/10.1063/1.3083299>.
- [41] Futatani, S., Horton, W., Benkadda, S., Bepamyatnov, I. O. and Rowan, W. L. (2010). Fluid models of impurity transport via drift wave turbulence, *Phys. Plasmas* **17**, p. 072512, <http://dx.doi.org/10.1063/1.3459062>.
- [42] Goniche, M., Artaud, J. F., Bourdelle, C., Bucalossi, J., Desgranges, C., Delpech, L., Devynck, P., Dumont, R., Ekedahl, A., Fedorczak, N., Garcia, J., Gil, C., Gunn, J., Klepper, C. C., Maget, P., Mazon, D., Meyer, O., Morales, J., Moreau, Ph., Nouailletas, R., Peysson, Y., Regal-Mezin, X., Reux, C., Saint-Laurent, F., Vezinet, D. and the WEST Team (2019). First Lower Hybrid Current Drive experiments on the WEST tokamak, preprint.
- [43] Guo, W., Wang, L. and Zhuang, G. (2017). Impact of impurities on zonal flow driven by trapped electron mode turbulence, *Nucl. Fusion* **57**, p. 126052, <https://orcid.org/0000-0002-5881-6139>.
- [44] Hazeltine, R. (2009). Research needs for magnetic fusion energy sciences, Report of the Research Needs Workshop (ReNeW), U. S. Department of Energy (Washington, DC).
- [45] Hoang, G. T., Horton, W., Bourdelle, C., Hu, B., Garbet, X. and Ottaviani, M. (2003). Analysis of the critical electron temperature gradient in Tore Supra, *Phys. Plasmas* **10**, pp. 405–413, <http://dx.doi.org/10.1063/1.1534113>.
- [46] Hong, S.-H., Kim, K.-M., Song, J.-H., Bang, E.-N., Kim, H.-T., Lee, K.-S., Litnovsky, A., Hellwig, M., Seo, D. C., Lee, H. H., Kang, C. S., Lee, H.-Y., Hong, J.-H., Bak, J. G., Kim, H.-S., Juhn, J.-W., Son, S.-H., Kim, H.-K., Douai, D., Grisolia, C., Wu, J., Luo, G.-N., Choe, W.-H., Komm, M., Van Den Berg, M., De Temmerman, G. and Pitts, R. (2015). Toward tungsten plasma-facing components in KSTAR: Research on plasma-metal wall interaction, *Fusion Sci. Tech.* **68**, pp. 36–43, <https://doi.org/10.13182/FST14-897>.
- [47] Horton, W. and Rowan, W. (1994). Impurity transport studies in the Texas Experimental Tokamak (TEXT), *Phys. Plasmas* **1**, p. 901, <http://dx.doi.org/10.1063/1.870749>.
- [48] Horton, W. and Ichikawa, Y. (1996). *Chaos and Structures in Nonlinear Plasmas* (World Scientific) ISBN:8177642340.
- [49] Horton, W. (1999). Drift waves and transport, *Rev. Mod. Phys.* **71**, p. 735, <http://dx.doi.org/10.1103/RevModPhys.71.735>.
- [50] Horton, W., Zhu, P., Hoang, G. T., Aniel, T., Ottaviani, M. and Garbet, X. (2000). Electron transport in Tore Supra with fast wave electron heating, *Phys. Plasmas* **7**, pp. 1494–1511, <http://dx.doi.org/10.1063/1.873969>.

- [51] Horton, W., Goniche, M., Peysson, Y., Decker, J., Ekedahl, A. and Litaudon, X. (2013). Penetration of lower-hybrid current drive waves in tokamaks, *Phys. Plasmas* **20**, p. 112508, <http://dx.doi.org/10.1063/1.4831981>.
- [52] Horton, W., Brookman, M., Goniche, M., Peysson, Y. and Ekedahl, A. (2017). RF Heating Technology Workshop and US/JAPAN Workshop on RF Physics, *High-frequency RF waves in lower-hybrid current drive* Santa Monica, California, USA, Sept. 5–8, 2017.
- [53] Horton, W. (2018). *Turbulent Transport in Magnetized Plasmas*, 2nd Edition (World Scientific, 2018), ISBN:978–981–3225–86–6.
- [54] Houshmandyar, S., Yang, Z. J., Phillips, P. E., Rowan, W., Hubbard, A. E., Rice, J. E., Hughes, J. W. and Wolfe, S. M. (2016). Temperature gradient scale length measurement: A high-accuracy application of electron cyclotron emission without calibration, *Rev. Sci. Instrum.* **87**, p. 11E101, <https://doi.org/10.1063/1.4955297>.
- [55] Houshmandyar, S., Yang, Z. J., Liao, K. T., Zhao, B., Phillips, P. E., Rowan, W. L., Cao, N., Ernst, D. R. and Rice, J. E. (2017). Electron profile stiffness and critical gradient length studies in the Alcator C-Mod Tokamak, *Division of Plasma Physics Meeting JP11.00092*, <http://meetings.aps.org/link/BAPS.2017.DPP.JP11.92>.
- [56] Houshmandyar, S., Austin, M. E., Brookman, M. W., Liu, Y., Rowan, W. L. and Zhao, H. (2018). Variable location channels to improve efficiency and precision for direct ∇T_e measurements and high spatial resolution T_e -profile measurements using electron cyclotron emission, *Rev. Sci. Instrum.* **89**, p. 10H109, <https://doi.org/10.1063/1.5035429>.
- [57] Ishizawa, A., Nakamura, Y. and Kishimoto, Y. (2016). 26th IAEA Fusion Energy Conference, IAEA CN-234, 17–22 October 2016, Kyoto International Conference Center, Takaragaike, Sakyo-ku, Kyoto 606–0001 Japan.
- [58] ITER Physics Expert Groups on Confinement and Transport and Confinement Modeling and Database, ITER Physics Basis Editors, and ITER EDA. (1999). *Nucl. Fusion* **39**, p. 2175, <http://epub.iaea.org/fusion>.
- [59] Kalmoni, N. M. E., Rae, I. J., Watt, C. E. J., Murphy, K. R., Forsyth, C. and Owen, C. J. (2015). Statistical characterization of the growth and spatial scales of the substorm onset arc, *J. Geophys. Res.: Space Phys.* **120**, pp. 8503–8516, <https://doi.org/10.1002/2015JA021470>.
- [60] Kim, Chang-Bae, An, Chan-Yong and Byunghoon, M. (2019). Reduction of edge plasma turbulence via cross-phase decrease by zonal fields, *Plasma Phys. Control. Fusion* **61**, p. 085024, <https://doi.org/10.1088/1361-6587ab2973>.
- [61] Kishimoto, Y., Tajima, T., Horton, W., LeBrun, M. J. and Kim, J-Y. (1996). Theory of self-organized critical transport in tokamak plasmas, *Phys. Plasmas* **3**, pp. 1289–1307, <http://dx.doi.org/10.1063/1.871754>.

- [62] Lang, P., Frigione, D., Geraud, Alarcon, T., Bennett, P., Cseh, G., Garnier, D., Garzotti, L., Köchl, F., Kocsis, G., Lennholm, M., Neu, R., Mooney, R., Saarelma, S., Sieglin, B. and JET–EFDA Contributors. (2013). ELM pacing and trigger investigations at JET with the new ITER–like wall, *Nucl. Fusion* **53**, p. 073010, <https://doi.org/10.1088/0029-5515/53/7/073010>.
- [63] Lau, C. K., Fulton, D. P., Holod, I., Lin, Z., Binderbauer, M., Tajima, T. and Schmitz, L. (2017). Drift–wave stability in the field–reversed configuration, *Phys. Plasmas* **24**, p. 082512, <https://doi.org/10.1063/1.4993630>.
- [64] Li, L., Liu, Y. Q., Loarte, A., Pinches, S. D., Polevoi, A. R., Liang, Y. and Zhong, F. C. (2019). Modeling 3D plasma boundary corrugation and tailoring toroidal torque profiles with resonant magnetic perturbation fields in ITER, *Nucl. Fusion* **59**, p. 096038, <https://doi.org/10.1088/1741-4326/ab2bca>.
- [65] Liewer, P. C. (1985). Measurements of microturbulence in tokamaks and comparisons with theories of turbulence and anomalous transport, *Nucl. Fusion* **25**, p. 543, <https://doi.org/10.1088/0029-5515/25/5/004>.
- [66] Loarte, A., Polevoi, A. R., Weyens, T., Liu, Y. Q., Li, L., Huijsmans, G. T. A., Artola, J., van Vugt, D. C., Liu, F., Sanchez, R., Reynolds–Barredo, J. M., Tribaldos, V., Medvedev, S. Y. and Futatani, S. (2018). Advances in modeling of plasma pedestal behaviour and ELM control in ITER reference plasma scenarios, Paper presented at 27th IAEA Fusion Energy Conference (FEC 2018), Gandhinger, India, <https://www.persistent-identifier.nl/urn:nbn:nl:ui:25-2eedee3e-5ff1-4be7-be96-68d8b289f567>.
- [67] Lüst, R. (1960). Magnetofluid dynamic shock waves, *Rev. Mod. Phys.* **32**, p. 706, <https://doi.org/10.1103/RevModPhys.32.706>.
- [68] Maggi, C. F., Delabie, E., Biewer, T. M., Groth, M., Hawkes, N. C., Lehnen, M., de la Luna, E., McCormick, K., Reux, C., Rimini, F., Solano, E. R., Andrew, Y., Bourdelle, C., Bobkov, V., Brix, M., Calabro, G., Czarnecka, A., Flanagan, J., Lerche, E., Marsen, S., Nunes, I., Van Eester, D., Stamp, M. F. and JET EFDA Contributors (2014). L–H power threshold studies in JET with Be/W and C wall, *Nucl. Fusion* **54**, p. 023007, <https://doi.org/10.1088/0029-5515/54/2/023007>.
- [69] Marcus, F. A., Roberto, M., Caldas, I. L., Rosalem, C. and Elskens, Y. (2019). Influence of the radial electric field on the shearless transport barriers in tokamaks, *Plasma Phys.* **26**, p. 022302, <https://doi.org/10.1063/1.5071437>.
- [70] Martin, Y. R., Takizuka, T. and the ITPA CDBM H–mode Threshold Database Working Group. (2008). Power requirement for accessing the H–mode in ITER, *J. Phys: Conference Series* **123**, p. 101033, <https://doi.org/10.1088/1742-6596/123/1/012033>.
- [71] Michoski, C., Horton, W. and Tamura, N. (2017), IFS Report.

- [72] Michoski, C. and Horton, W. (2019), IFS Report.
- [73] Miura, H., Zheng, L. and Horton, W. (2017). Numerical simulations of interchange/tearing instabilities in 2D slab with numerical model for edge plasma, *Phys. Plasmas* **24**, p. 092111, <http://dx.doi.org/10.1063/1.4993962>.
- [74] Miura, H., Miyazaki, J., Ide, M., Miyagi, D., Tsuda, M. and Yokoyama, S. (2018). Estimation method of optimal amount of overshooting current for temporal uniform magnetic field in conduction-cooled HTS coils, *IEEE Trans. on Appl. Superconductivity* **28**, pp. 1–5, <https://doi.org/10.1109/TASC.2018.2805688>.
- [75] Moradi, S., Fülöp, T., Mollen, A. and Pusztai, I. (2011). A possible mechanism responsible for generating impurity outward flow under radio frequency heating, *Plasma Phys. Control. Fusion* **53**, p. 115008, <https://doi.org/10.1088/0741-3335/53/11/115008>.
- [76] Moradi, S., Pusztai, I., Mollen, A. and Fülöp T. (2012). A possible mechanism responsible for generating impurity outward flow under radio frequency heating, *Plasma Phys. Control. Fusion* **53**, p. 115008, <https://doi.org/10.1088/0741-3335/53/11/115008>.
- [77] Nakmura, Y., Kobayashi, M., Yoshimura, S., Tamura, N., Yoshinuma, M., Tanaka, K., Suzuki, C., Peterson, B. J., Sakamoto, R., Morisake, T. and the LHD Experiment Group (2014). Impurity shielding criteria for steady-state hydrogen plasmas in the LHD, a heliotron-type device, *Plasma Phys. Control. Fusion* **56**, p. 075014, <https://doi.org/10.1088/0741-3335/56/7/075014>.
- [78] Nakmura, Y., Tamura, N., Kobayashi, M., Yoshimura, S., Suzuki, C., Yoshinuma, M., Goto, M., Motojima, G., Nagaoka, K., Tanaka, K., Sakamoto, R., Peterson, B. J., Ida, K., Osakabe, M., Morisake, T. and the LHD Experiment Group (2017). A comprehensive study on impurity behavior in LHD long pulse discharges, *Nucl. Mat. Energy* **12**, pp. 124–132, <https://doi.org/10.1016/j.nme.2016.11.005>.
- [79] Newell, P. T., Sotirelis, T., Liou, K., Meng, C.-I. and Rich, F. J. (2007). A nearly universal solar wind-magnetosphere coupling function inferred from 10 magnetospheric state variables, *J. Geophys. Res.* **112**, p. A0120, <https://doi.org/10.1029/2006JA012015>.
- [80] Ning, Z-X., Zhang, H-G., Zhu, X-Ming, Ouyang, L., Liu, X-Y., Jiang, B-H. and Yu, Da-R. (2018). 10000 Ignition-Cycle Investigation of a LaB6 Hollow Cathode for 3–5-Kilowatt Hall Thruster, *ARC* **35**, <https://doi.org/10.2514/1.B37192>.
- [81] Onishchenko, O. G., Pokhotelov, O. A., Horton, W., Smolyakov, A., Kaladze, T. and Fedun, V. (2014). Rolls of the internal gravity waves in the Earth’s atmosphere, *Ann. Geophys.* **32**, pp. 181–186, <https://doi.org/10.5194/angeo-32-181-2014>.
- [82] Peysson, Y., Decker, J., Morini, L. and Coda, S. (2011). RF current drive and plasma fluctuations, *Plasma Phys. Control. Fusion* **53**, p. 124028, <http://dx.doi.org/10.1088/0741-3335/53/12/124028>.

- [83] Peysson, Y., Decker, J., Nilsson, E., Atraud, J.-F., Ekedah, A., Goniche, M., Hillairet, J., Ding, B., Li, M., Bonoli, P. T., Shiraiwa, S. and Madi, M. (2016). Advances in modeling of lower-hybrid current drive, *Plasma Phys. Control. Fusion* **58**, p. 044008, <https://doi.org/10.1088/0741-3335/58/4/044008>.
- [84] Portone, A., Villone, F., Liu, Y., Albanese, R. and Rubinacci, G. (2008). Linearly perturbed MHD equilibria and 3D eddy current coupling via the control surface method, *Plasma Phys. Control. Fusion* **50**, p. 085004, <https://doi.org/10.1088/0741-3335/50/8/085004>.
- [85] Pratt, J. and Horton, W. (2006). Global energy confinement scaling predictions for the kinetically-stabilized tandem mirror, *Phys. Plasmas* **13**, p. 042513, <http://dx.doi.org/10.1063/1.2188913>.
- [86] Rowan, W. L., Bespamyatnov, Igor O. and Fiore, C. L. (2008). Light impurity transport at an internal transport barrier in Alcator C-Mod, *Nucl. Fusion* **48**, p. 105005, <https://doi.org/10.1088/0029-5515/48/10/105005>.
- [87] Schmitz, L., Ruskov, E., Deng, B. H., Gota, H., Gupta, D., Tuszewski, M., Douglass, J., Peebles, W. A., Binderbauer, M. and Tajima, T. (2014). Multi-channel Doppler backscattering measurements in the C-2 field-reversed configuration, *Rev. Sci. Instr.* **85**, p. 11D840, <https://doi.org/10.1063/1.4891415>.
- [88] Schmitz, L., Ruskov, E., Deng, B. H., Binderbauer, M., Tajima, T., Gota, H., Tuszewski, M. and the TAE Team Control of ion gyroscale fluctuations via electrostatic biasing and sheared $\mathbf{E} \times \mathbf{B}$ flow in the C-2 field-reversed configuration (2016). *AIP Conf. Proc.*, p. 1721, <http://dx.doi.org/10.1063/1.4944018>.
- [89] Sertoli, M., Angioni, C., Dux, R., Neu, R., Pütterich, Igochine, V. and the ASDEX Upgrade Team. (2011). Local effects of ECRH on argon transport in L-mode discharges at ASDEX Upgrade, *Plasma Phys. Control. Fusion* **53**, p. 035024, <https://doi.org/10.1088/0741-3335/53/3/035024>.
- [90] Sertoli, M., Dux, R., Pütterich, T. and the ASDEX Upgrade Team. (2015). Modification of impurity transport in the presence of saturated $(m, n) = (1, 1)$ MHD activity at ASDEX Upgrade, *Plasma Phys. Control. Fusion* **57**, p. 075004, <https://doi.org/10.1088/0741-3335/57/7/075004>.
- [91] Shen, Y., Dong, J-Q., Han, M. K., Sun, A. P. and Shi, Z. B. (2016). Isotope effects on instabilities driven by ion temperature gradient and tungsten ions in tokamak plasmas, *Nucl. Fusion* **58**, p. 076007, <https://doi.org/10.1088/1741-4326/aabcf9>.
- [92] Shen, Y., Dong, J-Q., Sun, A. P., Qu, H. P., Lu, G. M., He, Z. X., He, H. D. and Wang, L. L. (2016b). Isotope effects of trapped electron modes in the presence of impurities in tokamak plasmas, *Plasma Phys. Control. Fusion* **58**, p. 045028, <https://doi.org/10.1088/0741-3335/58/4/045028>.

- [93] Shen, Y., Dong, J-Q., Han, M. K., Sun, A. P. and Shi, Z. B. (2018). Isotope effects on instabilities driven by ion temperature gradient and tungsten ions in tokamak plasmas, *Nucl. Fusion* **58**, p. 076007, <https://doi.org/10.1088/1741-4326/aabcf9>.
- [94] Shibahara, K., Nosé, M., Fritz, T. A. and Niehof, J. (2010). A new generation mechanism of butterfly pitch angle distributions of energetic ions: Multiple pitch angle scattering in the stretched magnetic field, *J. Geophys. Res.: Space Phys.* **115**, p. A07229, <https://doi.org/10.1029/2010JA015281>.
- [95] Smith, J. P. and Horton, W. (1998). Analysis of the bimodal nature of solar wind-magnetosphere coupling, *J. Geophys. Res. Space Phys.* **103**, pp. 14917–14923, <https://doi.org/10.1029/97JA02861>.
- [96] Spencer, E., Horton, W., Mays, M. L., Doxas, I. and Kozyra, J. (2007). Analysis of the 3-7 October 2000 and 15-24 April 2002, geomagnetic storms with an optimized nonlinear dynamical model, *J. Geophys. Res.* **112**, p. A04S90, <https://doi.org/10.1029/2006JA012019>.
- [97] Spencer, E., Rao, A., Horton, W. and Mays, M. L. (2009). Evaluation of solar wind magnetosphere coupling functions during geomagnetic storms with the WINDMI model, *J. Geophys. Res.* **114** p. A02206, <https://doi.org/10.1029/2008JA013530>.
- [98] Sudo, S., Tamura, N., Suzuki, C., Muto, S., Funaba, H. and LHD Group (2012). Multiple-tracer TESPEL injection for studying impurity behavior in a magnetically-confined plasma, *Nucl. Fusion* **52**, p. 063012, <http://dx.doi.org/10.1088/0029-5515/52/6/063012>.
- [99] Tanaka, K., Michael, C. A., Vyacheslavov, L. N., Sanin, A. L., Kawahata, K., Akiyama, T., Tokuzawa, T. and Okajima, S. (2008). Two-dimensional phase contrast imaging for local turbulence measurements in large helical device, *Rev. Sci. Instrum.* **79**, p. 10E702, <http://dx.doi.org/10.1063/1.2988821>.
- [100] Tang, W. M. (1978). Microinstability theory in tokamaks, *Nucl. Fusion* **18**, p. 1089, <https://doi.org/10.1088/0029-5515/18/8/006>.
- [101] Tang, W. M., Bretz, N. L., Hahm, T. S., Lee, W. W., Perkins, F. W., Redi, M. H., Rewoldt, G., Zarnstorff, M. C., Zweben, S. J., Sydora, R. D., Dawson, J. M., Decyk, V. K., Naitou, H., Kamimura, T. and Abe, Y. (1989). Theoretical studies of enhanced confinement properties in tokamaks, *Plasma Phys. Control. Nucl. Fusion* **2**, 13 pp., <https://doi.org/10.2172/6527283>.
- [102] Troung, D. D. and Austin, M. E. (2014). High spatial resolution upgrade of the electron cyclotron emission radiometer for the DIII-D tokamak, *Rev. Sci. Instrum.* **85**, p. 11D814, <https://doi.org/10.1063/1.4889737>.
- [103] Villone, F., Liu, Y., Rubinacci, G. and Ventre, S. (2010). Effects of thick blanket modules on the resistive wall modes stability in ITER, *Nucl. Fusion* **50**, p. 125011, <https://doi.org/10.1088/0029-5515/50/12/125011>.

- [104] Villone, F., Barbato, L., Mastrostefano, S. and Ventre, S. (2013). Coupling of nonlinear axisymmetric plasma evolution with three-dimensional volumetric conductors, *Plasma Phys. Control. Fusion* **55**, p. 095008, <https://doi.org/10.1088/0741-3335/55/9/095008>.
- [105] Wade, M. R., Houlberg, W. A. and Baylor, L. R. (2000). Experimental confirmation of impurity convection driven by the ion-temperature gradient in toroidal plasmas, *Phys. Rev. Lett.* **84**, p. 292, <https://doi.org/10.1103/PhysRevLett.84.282>.
- [106] Wagner, F., Becker, G., Behringer, K., Campbell, D., Eberhagen, A., Engelhardt, W., Fussmann, G., Gehre, O., Gernhardt, J., Gierke, G. V., Haas, G., Huang, M., Karger, F., Keilhacker, M., Klüber, O., Kornherr, M., Lackner, K., Lisitano, G., Lister, G. G., Mayer, H. M., Meisel, D., Müller, E. R., Murmann, H., Niedermeyer, H., Poschenrieder, W., Rapp, H., Röhr, H., Schneider, F., Siller, G., Speth, E., Staebler, A., Steuer, K. H., Venus, G., Vollmer, O. and Yü, Z. (1982). Regime of improved confinement and high beta in neutral-beam-heated divertor discharges of the ASDEX Tokamak, *Phys. Rev. Lett.* **49**, pp. 1408–1412, <http://dx.doi.org/10.1103/PhysRevLett.49.1408>.
- [107] Wu, T., Nie, L., Xu, M., Yang, J., Chen, Z., Shi, Y., Wang, N., Li, D., Ke, R., Yu, Y., Gong, S., Long, T., Chen, Y., Liu, B. and J-TEXT Team 2. (2019). Effect of resonant magnetic perturbation on boundary plasma turbulence and transport on J-TEXT tokamak, *Plasma Sci. Technol.* **21**, p. 125102, <https://doi.org/10.1088/2058-6272/ab4369>.
- [108] Yamoto, S., Bonnin, X., Homma, Y., Inoue, H., Hoshino, K., Hatayama, A. and Pitts, R. A. (2017). Kinetic modeling of high- Z tungsten impurity transport in ITER plasmas using the IMPGYRO code in the trace impurity limit, *Nucl. Fusion* **57**, p. 116051, <https://doi.org/10.1088/1741-4326/aa7fa6>.